Carbon 193 (2022) 1–16

Contents lists available at ScienceDirect

Carbon

journal homepage: www.elsevier.com/locate/carbon

Structure-activity relationship of carbon nitride dots in inhibiting Tau aggregation

Yiqun Zhou [a, b, 1], Nabin Kandel [c, 1], Mattia Bartoli [d, 1], Leonardo F. Serafim [a, 1], Ahmed E. ElMetwally [a, 1], Sophia M. Falkenberg [a], Xavier E. Paredes [a], Christopher J. Nelson [a], Nathan Smith [c], Elisa Padovano [e], Wei Zhang [a], Keenan J. Mintz [a, f], Braulio C.L.B. Ferreira [a], Emel Kirbas Cilingir [a], Jiuyan Chen [a], Sujit K. Shah [a, g], Rajeev Prabhakar [a], Alberto Tagliaferro [e], Chunyu Wang [c], Roger M. Leblanc [a, *]

[a] Department of Chemistry, University of Miami, Coral Gables, FL, 33146, USA
[b] C-Dots, LLC, Miami, FL, 33136, USA
[c] Department of Biological Sciences, Rensselaer Polytechnic Institute, NY, 12180, USA
[d] Center for Sustainable Future, Italian Institute of Technology, Via Livorno 60, Turin, 10144, Italy
[e] Department of Applied Science and Technology, Politecnico di Torino, Italy
[f] School of Materials Science and Engineering, Georgia Institute of Technology, Atlanta, GA, 30332, USA
[g] Department of Chemistry, Mahendra Morang Adarsh Multiple Campus, Tribhuvan University, Biratnagar, 56613, Nepal

ARTICLE INFO

Article history:
Received 17 January 2022
Received in revised form
2 March 2022
Accepted 8 March 2022
Available online 10 March 2022

Keywords:
Carbon nitride dots
Tau aggregation
Alzheimer's disease
Reactive oxygen species
Blood-brain barrier

ABSTRACT

Due to the numerous failed clinical trials of anti-amyloid drugs, microtubule associated protein tau (MAPT) now stands out as one of the most promising targets for AD therapy. In this study, we report for the first time the structure-dependent MAPT aggregation inhibition of carbon nitride dots (CNDs). CNDs have exhibited great promise as a potential treatment of Alzheimer's disease (AD) by inhibiting the aggregation of MAPT. In order to elucidate its structure-activity relationship, CNDs were separated via column chromatography and five fractions with different structures were obtained that were characterized by multiple spectroscopy methods. The increase of surface hydrophilic functional groups is consistent with the increase of polarity from fraction 1 to 5. Particle sizes (1–2 nm) and zeta potentials (~-20 mV) are similar among five fractions. With the increase of polarity from fraction 1 to 5, their MAPT aggregation inhibition capacity was weakened. This suggests hydrophobic interactions between CNDs and MAPT, validated via molecular dynamics simulations. With a zebrafish blood-brain barrier (BBB) model, CNDs were observed to cross the BBB through passive diffusion. CNDs were also found to inhibit the generation of multiple reactive oxygen species, which is an important contributor to AD pathogenesis.

1. Introduction

Alzheimer's disease (AD) is an irreversible brain disorder that progressively worsens over time. It slowly destroys a person's memory and abilities to carry out simple tasks [1]. According to the National Institute on Aging, more than 5.7 million Americans may have dementia caused by AD and this number is predicted to triple by the year 2050. The life expectancy after a diagnosis of AD is generally 3–9 years and Alzheimer's Association states that it is the sixth leading cause of death in the United States [2]. Therefore, it is of great significance to prevent and treat AD. Regarding the pathogenesis of AD, the oldest hypothesis is the cholinergic hypothesis [3]. It proposed that AD was caused by a decline in the production of the neurotransmitter acetylcholine, which led to the development of acetylcholinesterase inhibitors for AD therapeutics [4]. In 1991 another influential hypothesis was proposed known as the amyloid cascade hypothesis. This hypothesis suggested that extracellular amyloid-β (Aβ) deposits were the fundamental cause of AD

* Corresponding author.
E-mail address: rml@miami.edu (R.M. Leblanc).
[1] All the authors contribute equally to this work.

https://doi.org/10.1016/j.carbon.2022.03.021
0008-6223/

[5]. In AD, β- and γ-secretases work together in a proteolytic process that causes amyloid precursor protein (APP) to be cleaved into smaller fragments [6]. One of these fragments, Aβ, aggregates to form amyloid fibrils, which deposit outside neurons in dense formations known as senile plaques [7], which is a pathological hallmark of AD brain. Moreover, the abnormal hyperphosphorylation and aggregation of a microtubule-associated protein tau (MAPT) are also implicated in the AD pathogenesis [8]. MAPT is an intrinsically disordered protein involved in the assembly and stability of microtubules. Under pathological conditions, it will undergo misfolding and aggregation. In addition, tau aggregates can further promote the aggregation of normal soluble tau in recipient cells, resulting in the propagation of tau pathology in a prion-like manner [9]. The neurotoxic accumulation of reactive oxygen species (ROS) was also recognized as a possible pathogenic mechanism of AD development [10]. However, due to the many failures of AD clinical trials, especially of anti-Aβ approaches, MAPT becomes a current focus for AD drug discovery.

Although many compounds show promises in cell cultures and AD animal models [11,12], the poor bioavailability of therapeutic agents in the brain hinders the translation of *in vitro* and *in vivo* tests to clinical trials. In order to improve the therapeutic efficacy, AD drugs usually have to be administered with high doses, which may lead to dose-dependent toxicity [13]. Additionally, many therapeutic agents that demonstrate to be effective in *in vitro* or *in vivo* studies are unable to cross the blood-brain barrier (BBB) to reach the brains due to their hydrophilicity, high surface charge, large molecular weight and particle size [14]. Also, the temporary disruption of endothelial tight junctions with osmotic pressure [15], microbubbles [16], and ultrasound [17] to facilitate BBB crossing is risky because it will damage the integrity of the BBB and cause an uncontrolled flux of medication and unwanted toxins into the central nervous system (CNS) [18]. Recently, nanotechnology is being explored for the development of nanomedicine that can both inhibit AD pathogenesis and cross the BBB.

Carbon dots (CDs) are one of the most promising nanomedicine and drug nanocarriers for AD drug development. They are widely available in our life and can be directly obtained from food and drink such as grilled food [19], honey [20], and beer [21], which suggests a great biocompatibility and reliability for treating human diseases. Also, compared to gold, silver NPs, and traditional quantum dots (QDs), CDs are novel carbon-based core-shell NPs with less toxicity due to the lack of metals. Compared to liposomes, CDs are smaller with sizes between 1 and 10 nm, which benefits the BBB penetration [22]. CDs are also easier to synthesize than carbon nanotubes, and they have a large surface-area-to-volume ratio which enhances drug loading capacity. More significantly, CDs display excellent photoluminescence (PL), which can be employed to track their pharmacokinetics in organisms with or without therapeutic agent cargos [23]. Although the fluorescence quantum yield (QY) varies among CD species due to different synthesis approaches, the highest value to date reached 93.3% [24], which is higher than that of most dyes widely used in biomedical fields such as Alexa (QY: 10–92%) and fluorescein (QY: 79%) [25]. As a unique class of CDs, carbon nitride dots (CNDs) possess all the aforementioned properties of general CDs [26,27]. Compared with other CDs, CND has a clearer core structure, which is amenable to computational modeling and MD simulations.

In addition, CDs in general possess many properties in favor of BBB penetration and AD treatment. For instance, CDs with small particle sizes, low surface charge and amphiphilicity are able to cross the BBB by passive diffusion [28]. On the contrary, CDs with large particle sizes, high surface charge and hydrophilicity can still overcome the BBB after surface modifications via active transport routes including receptor- and adsorption-mediated endocytosis and carrier-mediated transport [22,29,30]. Significantly, the BBB penetration ability of CDs won't be hampered by loading therapeutic agents [28], which was observed in a CND-based targeted therapy for glioblastoma [31]. Additionally, CDs alone can be considered as an effective nanodrug for the treatment of AD by inhibiting the activity of beta-secretase 1 (BACE1), production of APP, secretion, and fibrillation of Aβ [28,32,33]. Furthermore, molecular dynamic simulations demonstrated that the extended structures and flexibility of the Aβ monomers induced by the hydrophilic surfaces of black CDs (B-CDs), a CD species developed in our group, were probably the mechanism for the inhibition of Aβ fibrillation [33]. Considering the similarity between B-CDs and CNDs in terms of surface structure based on one of our recent studies [34], CNDs have the potential to interact with Aβ monomers just as B-CDs. And, to the best of our knowledge, CDs have never been studied in the MAPT pathogenesis of AD and even QDs and graphitic carbon nitride (g-C_3N_4) have been seldom investigated in this topic. With a deep delving in the process of MAPT aggregation, a bold idea is generated that whether and how CDs or CNDs to be specific can interact with tau monomers as Aβ monomers to prevent tau aggregation? Above all, with numerous failures of anti-Aβ approaches in AD clinical trials, more efforts should be made to study MAPT pathogenesis of AD.

Furthermore, the high levels of ROS in the brain of AD patients are deemed to contribute to AD pathogenesis. MAPT aggregation, Aβ peptide deposition and mitochondrial dysfunction are also relevant to oxidative stress. It has been reported that Aβ peptide deposition and MAPT aggregation can disturb the redox equilibrium, which leads to the production of excessive ROS [35,36]. Thus, the elimination of excess ROS to restore the redox equilibrium can help in AD treatment. The photocatalytic degradation of organic compounds has been introduced as an effective method to detect ROS such as superoxide radicals, hydrogen peroxide and singlet oxygen [36]. It is worth noting that many reports have mentioned the robust induction ability of CDs for the production of ROS. For example, Zhang et al. reported that N-doped CDs boosted the induction of ROS in the lysosome where the CDs tend to localize [37]. Moreover, two conjugated CDs were introduced as two-photon active photosensitizers to enhance the production of lethal ROS for nucleus-targeting photodynamic therapy [38]. On the other hand, few reports mentioned the ROS inhibition effect of CDs; for example, Chen et al. stated that CDs encapsulated in a self-healing hydrogel was able to scavenge excessive ROS [39]. Therefore, considering the oxidative stress imposed by excessive ROS to AD brains, it is of great significance to develop the CDs that inhibit or even consume ROS in AD treatment.

Herein, in this study, we combined a number of experimental techniques and molecular modeling to elucidate the structure-activity relationship of CND in its capability to inhibit MAPT aggregation. CNDs were synthesized by following our previously published procedures [26]. Then, CNDs were separated by column chromatography with a series of developing solvents of different polarities. Detailed characterizations of CNDs and separated fractions were conducted with various spectroscopies and microscopies, which revealed distinct structures of separated fractions. The MAPT aggregation inhibition capacity of each fraction was evaluated by a Thioflavin T (ThT) assay with a structure-property relationship proposed and validated by MD simulations. The capability to penetrate the BBB and excess ROS suppression were also investigated with a zebrafish BBB model and a photocatalytic degradation experiment, respectively. Overall, this work aims at the development of a transformative AD nanomedicine to target tau pathology by the elucidation of the structure-activity relationship of CNDs in MAPT aggregation inhibition.

2. Experimental section

2.1. Materials

Citric acid (99.5–100%) and quinine sulfate dihydrate (>99%) was purchased from VWR (West Chester, PA, USA). Urea (≥99.5%), ThT (98%) and dithiothreitol (DTT) (99%) were ordered from Sigma-Aldrich (St. Louis, MO, USA). The molecular tweezer CLR01 was prepared as described in the protocol elsewhere [40]. Rhodamine B (RhB) (95%) was bought from Alfa Aesar (Haverhill, MA). Tetrahydrofuran (THF) (≥99.8%) and methanol (≥99.9%) were provided by MP Biomedicals (Irvine, CA, USA). Heparin (223 units/mg) was procured from Celsus Laboratories, Inc. (Cincinnati, OH). The His-tagged tau protein was purified in the lab using established recombinant methods described elsewhere [41]. Deionized (DI) water was purified using a Modulab 2020 water purification system bought from Continental Water System Corporation (San Antonio, TX, USA). The purified water owned a surface tension of 72.6 mN m^{-1}, a resistivity of 18 MΩ cm, and a pH of 6.6 ± 0.3 at 20.0 ± 0.5 °C. All the chemicals were used without further treatment.

2.2. Characterizations

The as-prepared CNDs and separated fractions were characterized by UV/vis absorption spectroscopy in a 1 cm quartz cuvette (Starna Cells) using a Cary 100 UV–vis spectrophotometer (Agilent Technologies) in aqueous solution. PL emission spectra were recorded in aqueous medium (1-cm pathlength quartz cuvette) by a Horiba Jobin Yvon Fluorolog-3 with a slit width of 5 nm for both excitation and emission. The excitation-emission matrices were acquired with the software of Origin 9.1. The Fourier-transform infrared (FTIR) spectra were obtained using a PerkinElmer Frontier with a universal attenuated total reflectance (ATR) sampling accessary using air as the background. Thermogravimetric analysis (TGA) and derivative thermogravimetric analysis (DTG) analyses of CNDs and separated fractions were conducted using a thermomicrobalance (TG 209 F3 Tarsus, Netzsch, USA) while heating under a flow of nitrogen gas from 40 to 1000 °C at a rate of 10 °C/min. The particle morphologies were studied by combining atomic force microscopy (AFM) and transmission electron microscopy (TEM) with a 5420 atomic force microscope (Agilent Technologies) in tapping mode and a transmission electron microscope (1200×, JEOL, USA), respectively. Prior to either AFM or TEM screening, 5-min ultrasonication was conducted to reduce the self-aggregation. A nano series Malvern Zetasizer was applied for the zeta potential measurements. X-ray photoelectron spectroscopy (XPS) spectra were recorded by using a PHI 5000 Versaprobe (Physical Electronics, Chanhassen, MN, USA) scanning X-ray photoelectron spectrometer (monochromatic Al K-alpha X-ray source with 1486.6 eV, 15 kV, and 1 mA anode current) to investigate surface chemical composition. Raman spectra were collected using a Renishaw inVia (H43662 model, Gloucestershire, UK) equipped with a green laser line (514 nm) with a 50× objective. Raman spectra were recorded in the range from 250 to 3500 cm^{-1}.

2.3. Synthesis of CNDs

0.5 g of citric acid and 0.5 g of urea were dissolved in 25 mL of DI water and stirred vigorously overnight. Then the mixture was placed in a microwave oven of 700 W and heated for 7 min until all the water evaporated. The resultant black solid at the bottom of the beaker was collected, solubilized in about 15 mL of DI water and ultrasonicated for 30 min. The mixture was centrifuged for 15 min at 1500 rpm twice to remove any precipitation. The supernatant was then filtered through a 0.2 μm filter membrane to remove any remaining large particles. Then, the filtrate was dialyzed in a 100–500 Da molecular-weight cutoff (MWCO) dialysis tubing for 3 days in DI water with water changed every 24 h. In the end, CNDs in solid state were collected using a rotavapor with heating to 70–80 °C.

2.4. Separation of CNDs

CNDs were carefully separated with a series of solvents composed of THF and methanol with different volume ratios. Initially, 5 mg of the as-prepared CNDs were dissolved in 4 ml water which was transferred into a clean column packed with silica gel via wet method. THF was chosen as the developing solvent in the beginning while eluants were collected based on different colors and PL under the irradiation of a UV lamp (365 nm) until there was no more colored or photoluminescent eluants. Subsequently, the THF/methanol mixture (1:1, volume ratio) was used to continue the elution. When the eluant became clear and not photoluminescent, pure methanol was applied as the final developing solvent. Eventually, all the fractions of CNDs were concentrated with a rotavapor, dissolved in DI water, and lyophilized for 3 days to obtain solid samples.

2.5. Expression and purification of MAPT

The plasmid encoding a full-length tau protein with a 6xHis tag at the C-terminus was ordered from Gen-Script, USA. The plasmid was transformed into BL21-CodonPlus (DE3) RIPL competent cells and overexpressed following a standard overexpression protocol. Briefly, the bacterial culture was started by inoculating an isolated colony into 50 mL Luria broth (LB) with 100 μg/mL ampicillin, 50 μg/mL chloramphenicol and grown overnight in a shaking incubator at 250 rpm and 37 °C. The culture was palleted and again inoculated into 2L LB with the same antibiotics. The culture was grown with an optical density 600 nm (OD_{600}) of 1.0 and protein expression was initiated by adding 0.4 mM isopropyl β-D-1-thiogalactopyranoside (IPTG). After 4 h of expression at 250 rpm and 37 °C, cells were harvested by centrifugation and stored at −20 °C until purification. The cells were then extracted and purified using a Bio-Rad fast protein liquid chromatography (FPLC) system using a His-Tag Ni-NTA column. The purified His-tagged protein was characterized by sodium dodecyl sulfate-polyacrylamide gel electrophoresis (SDS-PAGE), mass spectroscopy, and then lyophilized and stored at −80 °C until use.

2.6. ThT assay

All the MAPT aggregation inhibition studies were performed on a Tecan Infinite M1000 microplate reader at 37 °C with orbital shaking at 250 rpm for over 60 h at an interval of 23 min. The ThT fluorescence intensity was monitored with excitation and emission wavelengths at 435 and 480 nm, respectively. A master mixture consisting of 10 μM His-tau protein, 2.5 mM dithiothreitol (DTT), 10 μM heparin and 10 μM ThT was set up using an assay buffer composed of 10 mM 4-(2-hydroxyethyl)-1-piperazineethanesulfonic acid (HEPES) and 100 mM NaCl at pH 7.4. Control experiments consisted of blank buffer with ThT, the master mixture without heparin, and the master mixture comprised of 100 μM Tweezer (CLR01, a known inhibitor of tau aggregation [42]). Serial dilutions of CNDs and separated fractions were performed to monitor the dose-dependent MAPT aggregation inhibition. Final data analyses and extraction of kinetic parameters were performed in Igor Pro program.

2.7. Computational details and MD simulations

The general structure of CND was created and optimized using the Gaussian 16 software package. The charges and electrostatic surface potentials (ESP) were computed at the B3LYP/6-31G(d) level of theory. The grimme D3 dispersion correction was used to account for the interactions between the multiple layers. The structure of tau protein was obtained from the protein data bank (PDB ID: 6HRE). The protein structure was optimized using all-atom MD simulation prior to the docking of CND. The Autodock Vina 1.5.6 software was used to evaluate the binding modes of CND onto the tau protein. The following two docking protocols were used: (1) rigid docking and (2) flexible docking. In the rigid docking, the structure of tau protein was kept fixed, while the CND was flexible. In the flexible docking, both tau and CND were allowed to change their conformations. The grid size was chosen to cover the entire peptide, and the spacing was kept to standard value (1.0 Å). An exhaustiveness value of 20 was used, which produced 20 poses with the highest relative binding affinities. The lowest energy pose was chosen as the starting point for the MD simulation. All the classic MD simulations were performed with the AMBER force field as implemented in GROMACS program. The system was inserted in a cubic 100 × 100 × 100 Å simulation box and filled with TIP3P water molecules. Sodium and chloride ions were added to simulate the physiological concentration of 0.154 mM and neutralize the system. The starting structures were then energy-minimized with a steepest descent algorithm for 3000 steps. The results of these minimizations produced the starting structure for the MD simulations. The MD simulations were then carried out with an isothermal-isobaric ensemble (*NPT*) without any geometric constrains. The long-range electrostatic interactions were calculated with the Particle-Mesh Ewald (PME) method. A constant pressure of 1 atm was applied with a coupling constant of 1.0 ps; peptide, CND, water molecules and ions were coupled to a bath at 300 K with a coupling constant of 0.1 ps. The timestep of 2 fs was used for the integration of the equations of motion. Finally, cluster analysis was performed to select the most representative structure along the 200 ns of simulation.

2.8. ROS measurements

All photocatalytic degradation experiments were carried out in a quartz cuvette with a 1-cm pathlength placed 10 cm in front of a solar simulator (Oriel Instruments, Newport Corporation) equipped with a high-power mercury-xenon light source (see Supporting Information, Fig. S9 for the spectrum). The cuvette was filled with 4 mL of aqueous solution (10 mg L^{-1}) of RhB and 0.6 mg of CNDs ultrasonically dissolved in the solution. Photocatalytic reactions were initiated by switching on the lamp, adjusting the power to 310 W, and recording the initial absorbances at 554 nm (RhB). Subsequently, in order to keep the concentration of photocatalysts and RhB steady throughout the whole UV/vis absorbance measurement process, instead of measuring out a few aliquots of samples, we directly used the cuvette containing both photocatalyst and RhB for UV/vis absorption measurements so that the sample volume used for this purpose was constantly 4 mL. Absorbances were read out every 10 min by a UV/vis spectrophotometer. According to the Beer-Lambert law, the absorbances reflect on the concentration changes of RhB. In addition, for further study of the effect of CNDs on ROS generation, CNDs were added to the system containing 4 mL of RhB aqueous solution (10 mg L^{-1}) and 12 mg of gel-like CDs (G-CDs) or a composite of G-CDs and g-C_3N_4(CD-g-C_3N_4) as described in our previous study [43]. UV/vis absorption spectrum was recorded each 10 min to compare the absorbances at 554 nm obtained from the system with or without CNDs. All the experiments were conducted three times each to ensure the accuracy and reproducibility of our results.

2.9. Zebrafish experiment

Wild-type (WT) zebrafish at 5 days post fertilization were obtained from the Zebrafish Core Facility at University of Miami. 10–50 mg/mL aqueous solutions of CND fractions were intravascularly injected into the heart of zebrafish previously anesthetized by 0.02% tricaine. After 10 min, the injected zebrafish were subjected for observation under a Leica SP5 confocal microscope under both white light and excitation at 405 nm. The animal care protocol for all the procedures used in this study was approved by the University of Miami Animal Care and Use Committee (protocol No.: 21–182 LF) and complies with the guidelines of the National Science Foundation.

3. Results and discussion

3.1. Separation of CNDs

The as-obtained CNDs were carefully separated by column chromatography. Selection of developing solvents was based on a preliminary TLC study shown in the Supporting Information, Fig. S1. With pure THF as the developing solvent, three fractions (F1, F2 and F3) were obtained. With THF/methanol (1:1, volume ratio), F4 was collected. Then, with pure methanol as the developing solvent, F5 was eventually acquired. After removal of organic solvents, all the five fractions were obtained as solid samples with a product yield of 3.0, 0.8, 7.5, 58.6 and 30.0% for F1–F5, respectively, showing a vast variation. Also, considering the increasing polarity of developing solvents, the polarity gradually increases from F1 to F5. In addition,

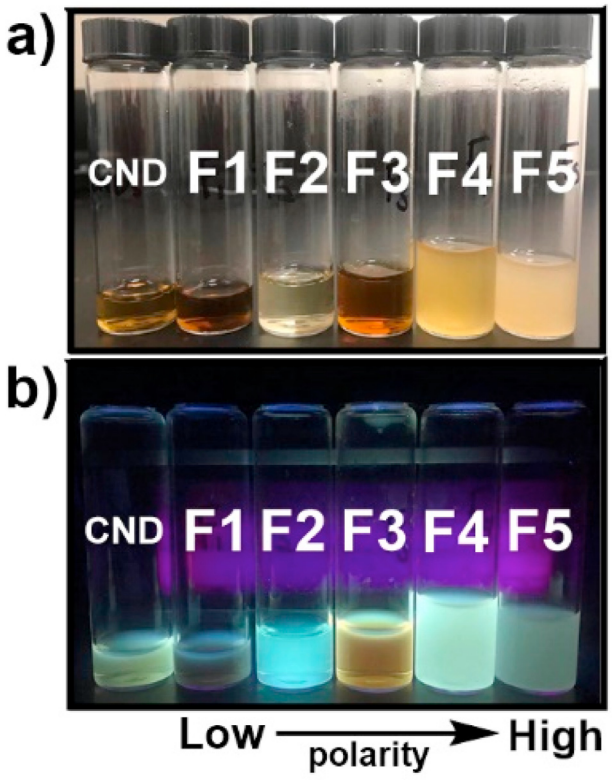

Fig. 1. Graphic illustration of F1, F2, F3, F4 and F5 with an increasing order of polarity, color and PL under white light (a) and UV irradiation (365 nm) (b).

Fig. 1 records the polarity, color, and PL of each fraction in aqueous media.

3.2. Characterizations of CND fractions

3.2.1. Optical properties

UV/vis absorption, differential reflectance, and fluorescence emission spectroscopies were performed on CNDs and separated fractions. UV/vis spectra of CNDs and separated fractions in Fig. 2a display four absorption peaks with wavelengths generally falling into four ranges (200–250, 250–300, 300–350, and >350 nm). In comparison, some absorption peaks disappear or shift in the spectra of separated fractions, revealing the structural differences of CND fractions. All the peak information of CNDs and separated fractions are recorded in the Supporting Information, Table S1. From the Supporting Information, Table S1, it is observed that in terms of absorption peaks, F1 resembles CNDs the most, which is followed by F3 and F2 regardless of slight shifts of different peaks due to the structural differences. Meanwhile, the peak at 200–250 nm is not clear in the spectrum of F4, which indicates a lack of C=C moieties on F4. Additionally, the peak at >350 nm, especially 410 nm for F2 and 415 nm for F3, indicates the moiety of NO_2 [44], and its redshift demonstrates the NO_2 is connected to a larger conjugated system within F2 and F3. Moreover, multiple peaks in the UV/vis absorption spectra of CNDs and separated fractions also account for the color and great light harvesting abilities of all the samples.

Furthermore, differential reflectance spectroscopy was performed on CNDs and five separated fractions using the same UV/vis spectrophotometer. Comparison of the spectra of five fractions in the Supporting Information, Fig. S2 reveals an increase of band gap between valence and conduction bands of CNDs with the increase of polarity (F1: 1.74 eV; F2: 1.86 eV; F3: 2.44 eV; F4: 2.80 eV; F5: 3.00 eV). Meanwhile, according to our previous study [45], the increasing band gap might be associated with a decreasing level of heteroatoms such as O and N from F1 to F5, which was confirmed later by the XPS measurements (Supporting Information, Fig. S3). Also, the enlargement of band gap increases the difficulty for electron transition and ROS induction. Considering the product yield of highly polar F4 and F5 that almost occupies 90% of CNDs, the overall CNDs behave inert to the environment. Therefore, ROS that are usually generated with CDs as photocatalysts will be inhibited [43,45], which, however, is beneficial for AD patients to avoid oxidative stress.

As to PL behaviors, it was observed in the fluorescence spectra (Fig. 3) that CNDs and all separated fractions exhibited excitation-dependent PL. Although the mechanism of excitation-dependent PL is constantly debated among theories of surface state, molecular state, core state and quantum confinement effect [23], the dominant voice is heterogeneity of different particles in terms of surface functionality. And it is hypothesized that in each CND fraction, there still exist many subfractions with subtle differences. The Supporting Information, Table S2, reveals their maximum excitation, emission wavelengths and fluorescence QY. At the same concentration of 1×10^{-3} mg/mL, compared with the overall CNDs, F1 and F5 share the same maximum excitation (375 nm) and emission wavelengths (452 nm), while when it comes to F2, F3 and F4, the two parameters are very different. In detail, the maximum excitation wavelengths of F2 and F3 are 400 nm while their maximum emission wavelengths red shift to above 500 nm. On the contrary, the maximum excitation/emission wavelengths occur blueshift to 325/427 nm, respectively, for F4. Additionally, a concentration-dependent PL behavior was observed in F2, F3 and F4, and they all exhibited a redshift when their concentrations were increased (Fig. S5), which might stem from self-aggregation [46]. Thus, the huge difference in PL of different fractions is likely due to the presence of distinct surface states that result from surface structural differences [45]. A composition of these fractions contributes to an excitation-dependent PL of the overall CNDs that favors their applications in biological matrixes to avoid the interference of intrinsic autofluorescence.

Moreover, the fluorescence QY of CNDs and each fraction was calculated using quinine sulfate as a standard reference. The QY values are recorded in the Supporting Information, Table S2. The QY of the overall CNDs is a mean QY attributed by each fraction. Compared to CNDs, separated fractions displayed a higher QY such as F2, lower QY such as F1, F4 and F5, or a similar QY such as F3, and the differences in QY can be ascribed to the same reason for different PL properties. In fact, it is not uncommon to observe that some fractions of CDs possess a higher QY than that of the overall CDs [47], and it seems to provide an alternative methodology to obtain CDs with higher QY via purification and separation.

3.2.2. Structural investigations

Structures of CNDs and separated fractions were initially investigated using FTIR and TGA. According to the FTIR spectra exhibited in Fig. 2b and functional moieties identified in the Supporting Information, Table S3, distinct structures of CND fractions were presented. In general, although minor variations exist and some peaks are not detectable, most peaks are easy to be identified

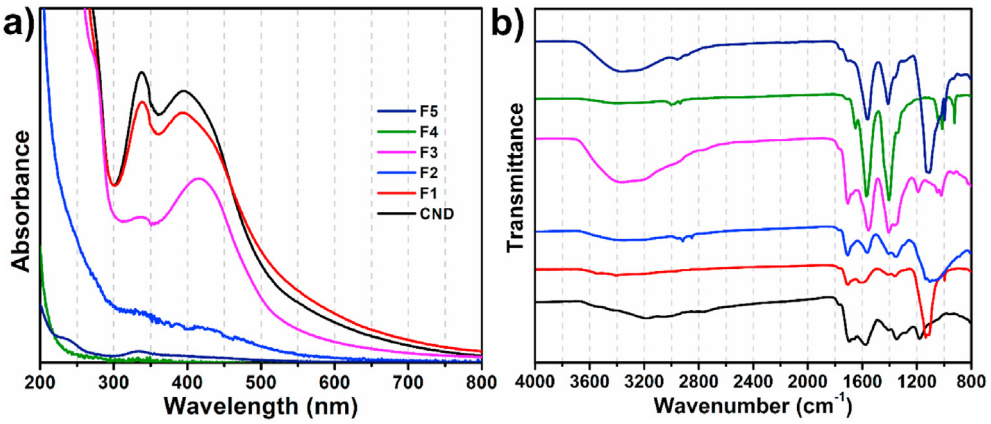

Fig. 2. Physicochemical characterizations of CNDs and separated fractions. (a) UV/vis absorption spectra of CNDs, F1, F2, F3, F4, and F5 at 0.1 mg/mL; (b) FTIR spectra with ATR technique and air as background.

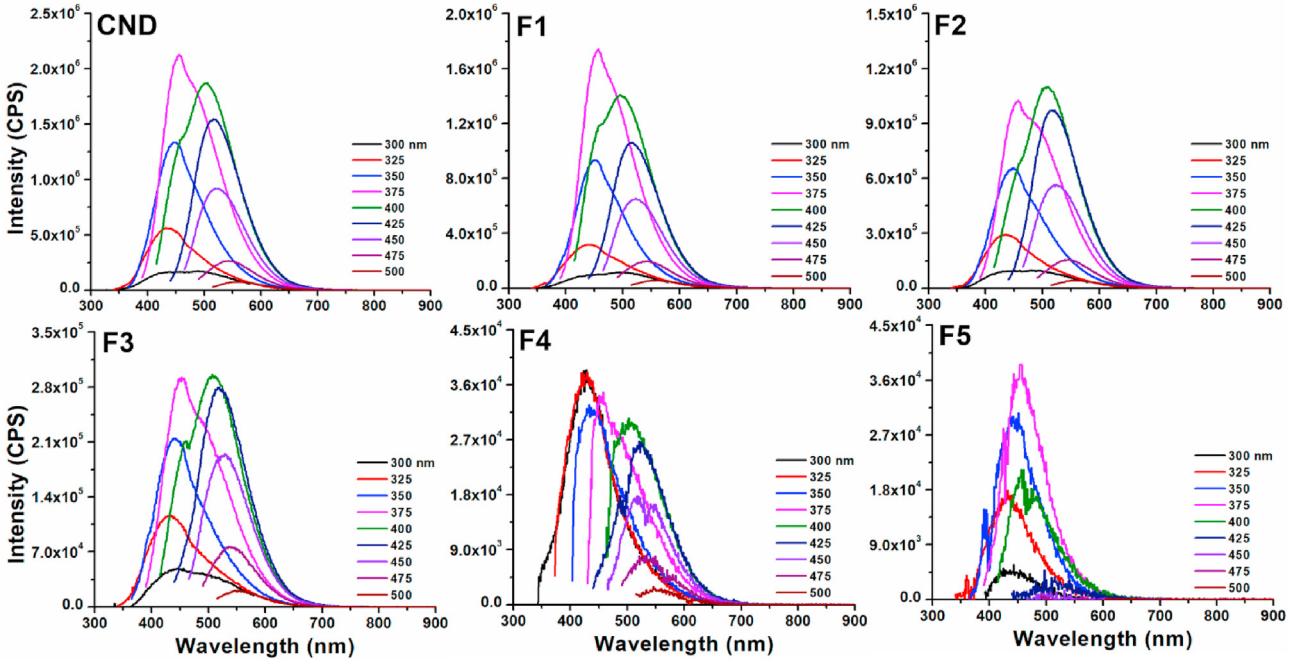

Fig. 3. The fluorescence spectra of the overall CNDs, F1, F2, F3, F4, and F5 at 1.0×10^{-3} mg/mL.

according to the IR Spectrum Table & Chart from Sigma-Aldrich. Additionally, structures including C═C, C═O, C═N, and NO_2 identified by FTIR spectral peaks are consistent with that shown in UV/vis absorption spectra. It is noteworthy that although C═C was not detected in F4 by the UV/vis absorption spectroscopy, it is identified by the FTIR spectrum, which might suggest that F4 possesses a low content of C═C.

In terms of TGA of each fraction exhibited in Fig. 4, functional moieties can be identified and quantified in each fraction based on their own thermal stabilities and decomposition temperatures. In addition, citric acid and urea, two precursors of CNDs, were also decomposed in comparison to each fraction and their TGA spectra are presented in the Supporting Information, Fig. S6a. However, in the range of 150–220 °C, a sole sharp peak shown in the DTG spectrum (Supporting Information, Fig. S6b) reveals that citric acid was quickly transformed into aconitic acid, itaconic acid and anhydrous itaconic acid while releasing H_2O and CO_2 [48]. Moreover, according to Stradella et al., decomposition of urea has three steps [49], which is consistent with our experimental results (Supporting Information, Fig. S6c), namely formation of biuret (106–258 °C), formation of cyanuric acid while decomposing urea into ammonia gas and cyanic acid, and producing a small amount of ammelide (258–358 °C), and decomposition of cyanuric acid (358–428 °C). Thus, considering these complex reactions occurring to citric acid and urea, it is unwise to directly compare the TGA results of citric acid and urea to that of CNDs and each fraction.

Instead, the literature references recording the TGA measurements of a wide range of chemicals and materials were used to identify and compare each functional moiety on CNDs and separated fractions qualitatively and quantitatively. Based on our previous studies on the TGA of CNDs, mass loss at 40–168, 168–338, 338–448, 448–618 and 618–688 °C represents evaporation of water molecules [50–52], decomposition of oxygen-containing functional moieties [53,54], and decomposition of carbon nitride (C_3N_4) structures, respectively [34]. With aforementioned references and DTG shown in Fig. 4 taken into consideration, the decomposition analyses of CNDs and separated fractions are as follows. The peak at 40–96 °C indicates water adsorbed on the

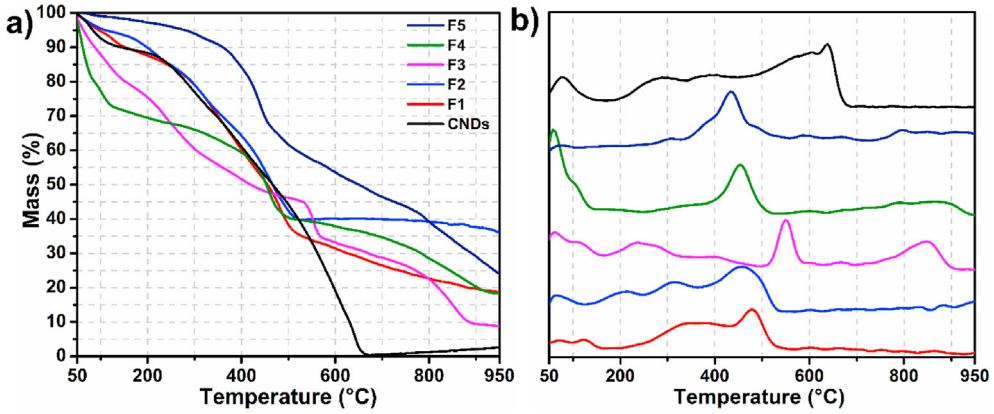

Fig. 4. (a) TGA and (b) DTG of CNDs and separated fractions.

surface or trapped in all fractions while the peak at 96–160 °C represents the loss of water formed through dehydration condensation reactions of alcoholic –OH [55], which varies among CNDs and F1–F5 as shown in Fig. 4. Moreover, 160–250 °C is ascribed to the decomposition of edge-plane oxygen-containing functional moieties including epoxy, carboxyl (-COOH) and carbonyl (C=O) groups while forming phenol groups and releasing CO and CO_2 [55,56]. The stage at 250–333 °C depicts the dissociation of stable O-containing functional moieties and sublimation of carbon framework [55]. The stage of 333–523 °C suggests decomposition of amines while releasing ammonia gas [57,58]. The last stage of 550–1000 °C is attributed to the decomposition of graphene and heptazine-based C_3N_4 structures into carbon and nitrogen containing gases [59–61], and the heptazine-based units have been confirmed by NMR measurements in one of our previous studies [26]. As to the calculation method, considering adsorbed water and remnant in the end of thermal decomposition which is presumed to be silica gel used in the column chromatography, the mass loss in each stage of CNDs and each fraction was recalculated by dividing the mass loss read from TGA by the sum of mass loss except that of adsorbed water and remnant at 1000 °C. After recalculation, the content of each functional moiety on CNDs and each fraction is listed in Table 1. In comparison, the content of alcoholic –OH among five fractions are in the order of F2(15%)>F3(13%) = F4(13%) >F1(9%)>F5(4%); the content of O-containing functional moieties and their connected carbon framework among five fractions are in the order of F1(44%)>F3(28%)>F2(26%)>F4(15%)>F5(5%); the content of amines are in the order of F2(48%)>F4(36%)>F5(35%) >F1(27%) = F3(27%); the content of "core" are in the order of F5(56%)>F4(36%)>F3(32%)>F1(20%)>F2(11%); on the contrary, the content of "shell" in five fractions are in the order of F2(89%) >F1(80%)>F3(68%)>F4(64%)>F5(44%). Also, most importantly, the content of hydrophilic functional moieties including alcoholic –OH and amines on the "shell" of each fraction was calculated, which is in the order of F5(89%)>F4(77%)>F2(71%)>F3(59%)>F1(45%). It generally matches the polarity strength of five fractions. And the reason why O-containing functional moieties are not included in the calculation of the surface content of hydrophilic functional moieties is due to inability to separate carbon framework from O-containing functional moieties. Moreover, the content of each functional moiety on CNDs is close to that on F4 and F5 considering their high contents in the overall CNDs and the measurements provide important information in modeling CNDs in preparation for the investigation of the interactions between CNDs and MAPT via MD simulations.

In order to further study the structures of CND fractions and understand the interactions between CNDs and MAPT, XPS and Raman spectroscopy were employed. Due to the low product yield of F2, further characterizations were carried out only with F1 and F5, the two most different fractions in terms of polarity. As a result, XPS spectra exhibited in the Supporting Information, Fig. S3, show the oxygen/carbon and nitrogen/carbon ratios in F1 are 78% and 14% and both of them are higher than that in F5 which are 56% and 4%, respectively. In addition, C1s spectrum displayed in the Supporting Information, Fig. S4 and Table 2 show the absence of sp^3 hybridized carbon but presence of sp^2 hybridized carbon (284.8 eV) [34] revealing a content of 61.6% and 68.4% for F1 and F5, respectively, which is consistent with aforementioned TGA results. The peaks attributed to carbon atoms bonded to heteroatoms are also present as C-X (X = N, O; 285.9 eV), C=O (288.8 eV), and COOH (288.9 eV) [34]. O1s signals show the presence of hydroxyl (531.5 eV), carbonyl (532.2 eV), and carboxylic functionalities (535.8 eV) [62]. Interestingly, carbonyl functionalities are present in a larger amount compared to C–O and COOH residues. N1s signals are composed of two peaks corresponding to nitride (398.9 eV), and

Table 1
Functional moiety identification and quantification by TGA measurements.

	Adsorbed H_2O	-OH, alcohol	C=O COOH C–O	amines	"shell" %	C_3N_4 unit graphene ("core" %)	remnant effective mass %	OH % (recalculation)	amine % (recalculation)	C=O %+ COOH %+ C–O % (recalculation)	"shell" % (recalculation)	"core" % (recalculation)	OH + NH_2% on the "shell"
F1	(40 –96 °C) 5%	(96 –168 °C) ≤7%	(168 –433 °C) ≥35%	(433 –563 °C) ≥21%	63%	(563–1000 °C) 16%	16%	9%	27%	44%	80%	20%	45%
F2	(40 –127 °C) 6%	(127 –248 °C) ≤9%	(248 –363 °C) ≥16%	(363 –543 °C) ≥29%	54%	(568–1000 °C) 7%	33%	61%	15%	48%	26%	89%	11%	71%
F3	(40 –90 °C) 10%	(90 –163 °C) ≤11%	(163 –343 °C) ≥23%	(343 –593 °C) ≤22	56%	(593–1000 °C) 26%	8%	82%	13%	27%	28%	68%	32%	59%
F4	(40 –91 °C) 21%	(91 –152 °C) 8%	(152 –363 °C) ≤9%	(363 –528 °C) ≤22%	39%	(528–1000 °C) 22%	18%	61%	13%	36%	15%	64%	36%	77%
F5	(40 –111 °C) 1%	(111 –268 °C) ≤3%	(268 –333 °C) ≤4%	(333 –473 °C) ≤27%	34%	(473–1000 °C) 43%	22%	77%	4%	35%	5%	44%	56%	89%
CNDs	(40 –122 °C) ≤9%	(122 –168 °C) ≤2%	(168 –338 °C) 18%	(338 –448 °C) 18%	38%	(448–1000 °C) 53%	0	91%	2%	20%	20%	42%	58%	57%

Table 2
Output of XPS analysis for carbon, oxygen, and nitrogen.

Fraction	Carbon (%)				Oxygen (%)			Nitrogen (%)	
	C sp^2	C-X (X = N, O)	C=O	COOH	C–O	C=O	COOH	Nitride	-NH_2
F1	61.6	13.5	19.0	5.9	31.1	57.3	11.6	18.2	81.8
F5	68.4	8.1	13.7	9.8	35.0	51.4	13.6	41.6	58.4

NH_2 residues (400.1 eV) [62]. The relative intensity of these two peaks agreed with the trend observed in TGA. Furthermore, the Raman spectra of both fractions (Supporting Information, Fig. S7) show very intense PL. While no other peaks can be detected in the spectrum of F5, the spectrum of F1 exhibits weak peaks in the region of sp^2 carbon bonds (1000-1800 cm^{-1}, D and G peaks).

Based on the outcomes of XPS, FTIR, TGA and MALDI-TOF analyses, a comprehensive model of the CND is proposed. MALDI-TOF suggests the presence of fragments of up to around 861 g/mol while XPS, FT-IR and TG proved the presence of materials with a high degree of functionalization. This in fact excludes a pure triazine-like structure and suggests structures of greater variability. Hence, we hypothesize a multi-layered structure of CND as reported in Fig. 5. According to Mintz et al. [34], triazine layers represent the outer layers of CNDs while their cores are mainly composed of N-doped graphene-like layers. According to the Lerf-Klinowsky model [63], the residual functional groups, such as carboxylic, carbonyl and amino/hydroxyl residues, are present on the edges of the planes. The XPS analysis suggests that nitrogen is present as amino groups or directly inserted in six-member-ring structures.

Furthermore, regarding the possible structures of F1 and F5, a unique assignation is highly speculative due to the great number of possible isomers. Nevertheless, we suggest a possible family of graphene layers for F1 and F5 with more polar groups on the shell of F5 than F1 (TGA data, Table 1). Accordingly, we hypothesized a triazine-like layered structure for F5 with disorganized core layers. The massive functionalization of F1 core layers could lead to that the polar functionalities strongly interact with each other, producing a shell-core interphase unipolar aromatic system that could pile triazine layers in a more efficient way. Based on the model reported in Fig. 5, the differences in the core layers may be accountable for the different interactions with tau. As reported in Fig. 10, the deformation of planarity of triazine layers allowed their interactions with protein residues. Accordingly, different core layers induced modifications of d_1 and d_3 distances with a concurrent modification of space arrangement of triazine layers and interactions with tau domains.

3.2.3. Morphological studies

AFM was applied to measure the mean particle size perpendicular to the x-y plane, namely along the z axis, of each fraction deposited on individual mica slides. According to Fig. 6, size distributions show minor aggregation in each fraction and the mean particle sizes of F1–F5 along the z axis are between 1 and 2 nm. Subsequently, TEM images of five fractions were recorded as Fig. 7 that displays similar particle sizes of F1–F5 on the x-y plane to that obtained along the z axis. Thus, the combination of AFM and TEM results reveals that all fractions are CNDs with nearly spherical shapes. To be specific, the size distribution histograms show the sizes of five fractions are 1.7 ± 0.6 (F1), 1.3 ± 0.5 (F2), 1.5 ± 0.7 (F3), 1.7 ± 0.7 (F4), and 1.9 ± 0.8 (F5) nm, respectively. The unspecific pattern of particle size variation reminds us that the separation was not based on particle sizes.

However, considering the nanoscale particle sizes, a quantum confinement effect may apply to CNDs and all the separated fractions. In QDs, quantum confinement allows for QDs to be assigned to specific incident energy levels based on particle size. As QDs become smaller, quantum confinement increases the effective bandgap, leading to a blue shift of the fluorescence emission spectra [64]. With these facts taken into account, the fluorescence emission data of all the separated fractions (Table S2) were reviewed. It is observed that the maximum fluorescence emission wavelength red shifts in the order of F4<F1<F5<F3<F2, which, however, doesn't match the particle size increases in the order of F2< F3<F1 ≈ F4<F5. Therefore, quantum confinement effect may be present in the PL behaviors of CNDs, but it is definitely not predominant. In addition, the difference in particle size among all the fractions are negligible and similar particle sizes exclude the effect of particle size on the interactions between CNDs and MAPT.

3.2.4. Zeta potential measurements

Zeta potential is an important parameter that determines the surface electrical properties. In comparison, zeta potential values of CNDs and five fractions shown in the Supporting Information, Table S4, are similarly negative, which suggests similar moderate colloidal stabilities and electrostatic interactions between each

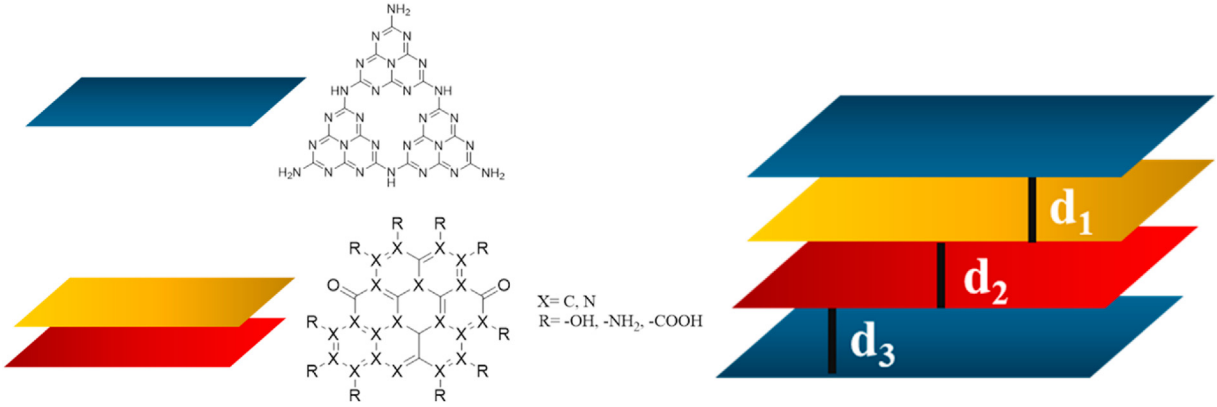

Fig. 5. Hypothetical multi-layered model of CND based on XPS, FTIR, TGA and MALDI-TOF analyses.

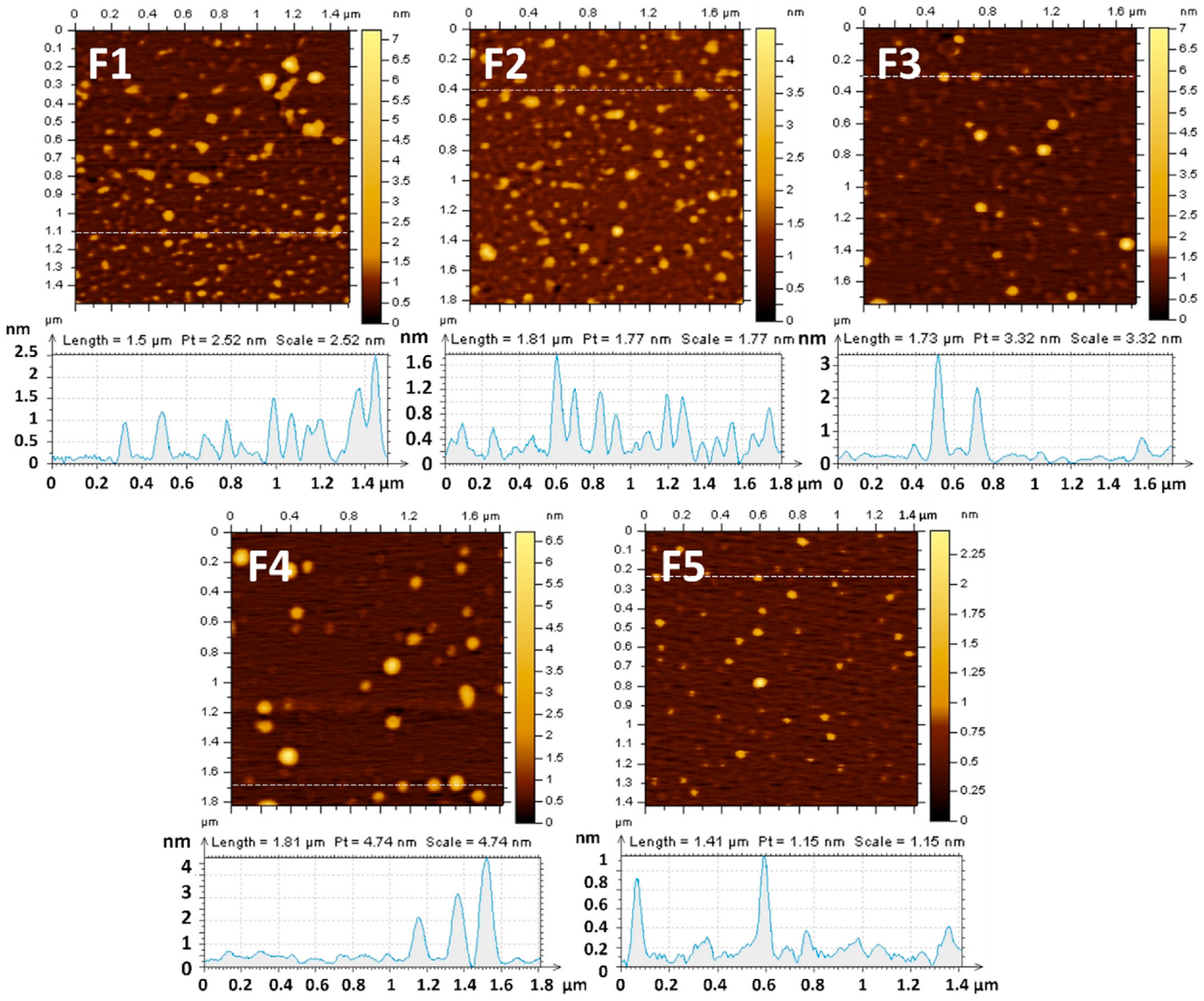

Fig. 6. AFM images of F1–F5 with their respective size distributions.

CND fraction with MAPT. Also, the results can be used to explain the minor aggregation of CND fractions displayed in AFM and TEM images in Figs. 6 and 7.

3.3. *MAPT aggregation inhibition with carbon nitride dots and their fractions*

The ThT fluorescence assay demonstrates that CNDs and their fractions inhibited tau aggregation in a dose-dependent manner (Fig. 8). Data were normalized on a scale from 0 to 1 with a baseline correction at zero and the maximum uninhibited tau aggregation at 1 to facilitate comparison among different concentrations of inhibitors. The lag time (t_{lag}) and the time at the half completion of the aggregation process (t_{half}) were evaluated by fitting a sigmoidal function with each kinetic trace. The uninhibited tau aggregation kinetics followed a multi-step secondary nucleation dominated pathway with a t_{lag} of 13.4 ± 0.2 h and a t_{half} of 18.9 ± 0.1 h. The elongation rate constant was estimated to be 0.358 h^{-1} with an amplitude of 0.965 h^{-1} assuming a dimeric size of the primary and secondary nucleus. As the concentration of inhibitors increased, the t_{half} increased while the elongation rate constant decreased except for highly polar fractions like F4 and F5 which showed biphasic dependance of these parameters. The highest concentration of inhibitors (143 µg/ml) almost completely inhibited the aggregation in all CND fractions except F4 and F5. This prevented the extraction of exact parameters for this concentration. The kinetic data reported here is of sufficient quality and reproducibility as confirmed by four duplicates of each measurement. The detailed kinetics parameters are summarized in the Supporting Information, Tables S5–7. Indeed, in comparison to the control groups, when a low concentration of CNDs or their fractions was added to incubate with MAPT, some enhancement was observed, which suggests that CNDs or their fractions might induce an aggregation nucleus that appears early in the amyloid formation pathway [65]. However, after the concentration was increased, a clear dose-dependent manner was shown in the tau aggregation inhibition of CNDs and each fraction, which indicates strengthened nanoparticle/tau interactions.

In addition, based on each ThT fluorescence kinetic trace, the

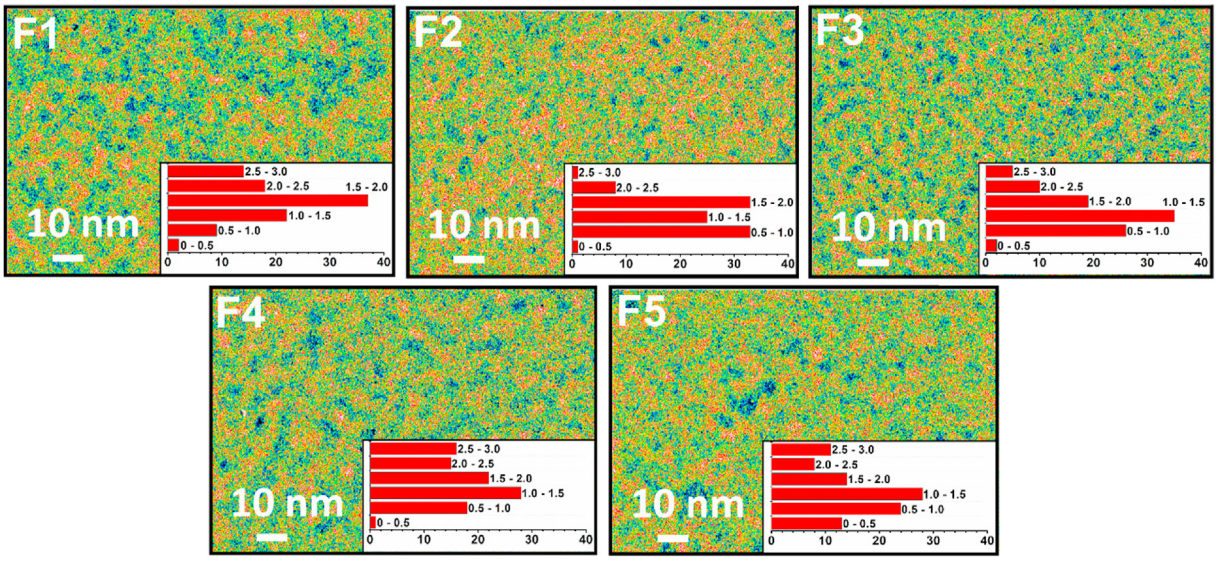

Fig. 7. TEM images of F1–F5 with size distribution histograms in nanometer as insets.

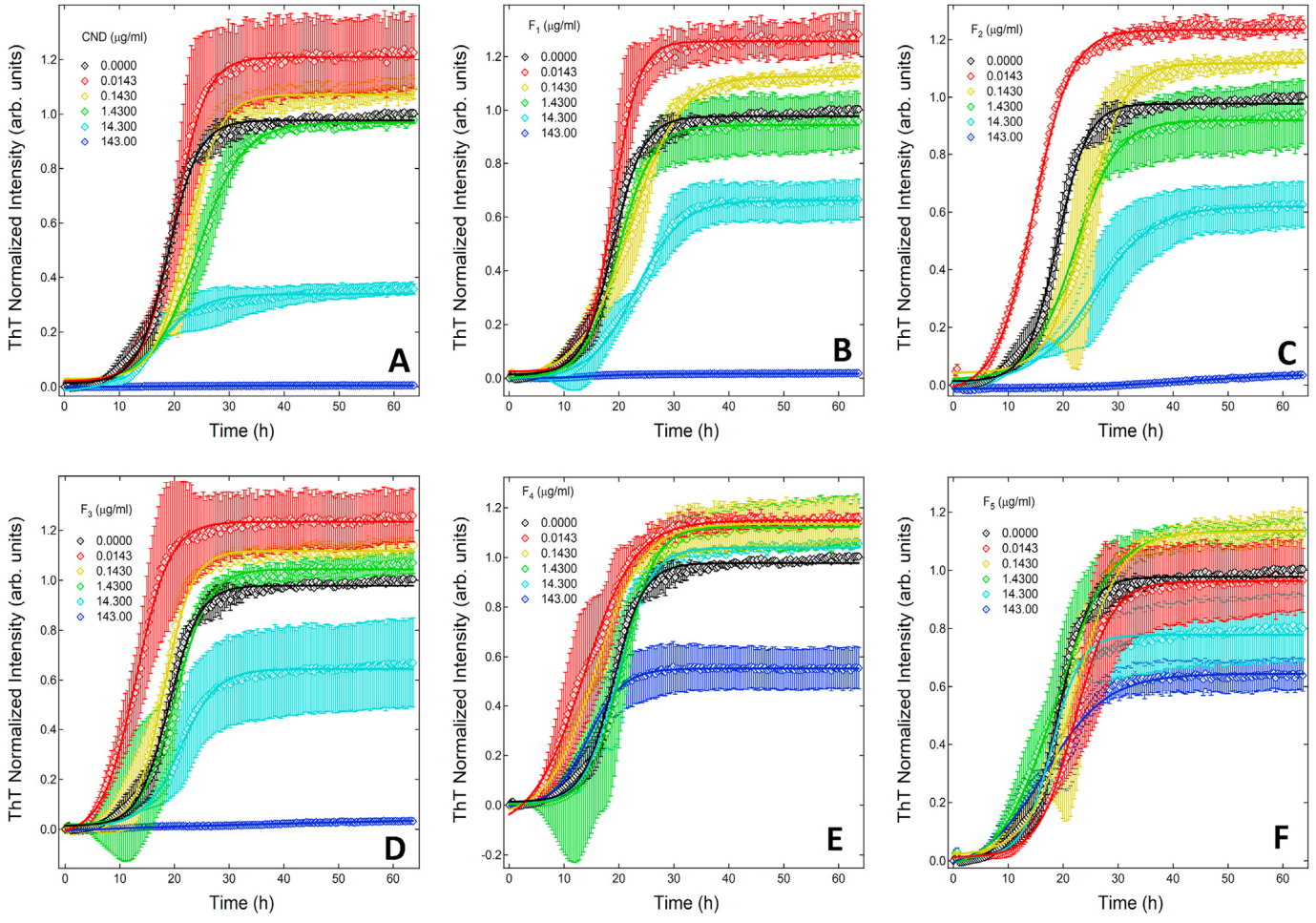

Fig. 8. Tau aggregation inhibition kinetics of CNDs and their fractions, F1, F2, F3, F4, and F5 as shown in graphs (A), (B), (C), (D), (E), and (F) respectively as monitored by a ThT fluorescence assay. The uninhibited tau aggregation control is shown in black and CNDs or their fractions inhibiting tau aggregation at various concentrations are shown in red (0.0143 μg/mL), yellow (0.143 μg/mL), green (1.43 μg/mL), cyan (14.3 μg/mL), and blue (143 μg/mL).

percentages of tau aggregation inhibition for different inhibitors were determined. The half-maximal inhibitory concentration (IC50) for CNDs (F0), F1, F2 and F3 was then interrogated by fitting a sigmoidal function with these inhibition percentage values as a function of the concentration of inhibitors in a semi-log scale (Supporting Information, Fig. S8). According to these IC50 analyses, it is noteworthy that the overall CNDs (F0) show the best effect on the tau aggregation inhibition compared to separated fractions. Additionally, CNDs were able to completely suppress the tau aggregation at a final concentration of 143 μg mL^{-1}. As the polarity increases from F1 to F5, the inhibition potency decreases. The overall CNDs have the lowest IC50 ~ 8 μg/mL that falls into a typical range for small molecule drug candidates. With the increase of hydrophilic functional moieties like −OH groups and amines, the IC50 value increases from F1 to F5. Our results indicate that the overall IC50 ranking among CNDs and their fractions follow the order CND < F1 ≈ F2 ≈F3 < F4 < F5 with the most polar fractions F4 and F5 displaying the highest IC50 > 143 μg/mL. The weak inhibition potency of F4 and F5 prevented precise calculations of their IC50 values. The calculated IC50s of CNDs (F0) and separated fractions are summarized in the Supporting Information, Table S8. In addition, it is noteworthy that the overall CNDs show the lowest IC50, which contradicts with our previous statement. Since F4 and F5 are the major components of CNDs, the overall CNDs were not supposed to exhibit a higher inhibition capacity than any separated fractions unless there exists a synergy of different tau aggregation inhibitors including all the fractions or the π-π stacking between different fractions enhanced the surface area, which strengthened the interactions between CNDs and tau, which will be investigated in our future work.

3.4. Computational modeling

Different from typical CDs, the “core” of CNDs possesses C atoms double bonded to N atoms with high N:C ratios in their structures [66]. These CNDs are built from C and N-containing heterocycles with triazine or heptazine rings linked through sp^2 bonded nitrogen atoms [66]. Our spectroscopic measurements indicate the presence of triazine or heptazine rings in the “core” of CNDs and separated fractions. The same spectroscopic measurements also indicated the presence of O-containing functional moieties. These moieties such as carboxyl and hydroxyl groups may be located on the edge of poly-C_3N_4 units endowing them with good water solubilities and high polarities. Since the exact location of these functional moieties cannot be pinpointed, we may as well firstly model the CND with a more assured structure such as the “core” to study the interactions between tau protein and the “core”, because, according to TGA, the “core” occupies almost 60% of the molar mass of CND. Also, since the overall CNDs showed the best performance in MAPT aggregation inhibition, our MD simulation study will cling to the “core” of the overall CND instead of separated fractions.

Therefore, our computational modeling of the CND takes into account that heptazine rings are the building block of CND core [67]. The s-triazine rings in the structure of CNDs have been previously confirmed by spectroscopic techniques such as: solid-state ^{13}C NMR, UV/vis absorption, and FTIR [26]. Also, the C_3N_4 structures in CNDs were validated by XPS data [34]. As stated previously, according to both TGA and DTG analyses, the “core” occupies 60% of the molar mass of CND. Moreover, the peaks observed at 215 and 604 g/mol in MALDI (TOF) mass spectrometry spectrum, are another evidence of the presence of s-heptazine and triple-heptazine rings which are the major constituents of the core of CND [26]. Although these peaks don't represent the real molar mass of CNDs, they can indicate the molar mass of the most repeated units released by weak bond breakages as the dispersive π-π stacking. Finally, based on AFM and TEM measurements (Figs. 6 and 7), the average diameter obtained for the CNDs is 1–2 nm.

Our CND model follows the layer model proposed in the literature [68], and 4 triple-heptazine layers are stacked to form the core of CND (Fig. 9). After geometry optimization, the CND has a diameter of 1.45 nm. Each layer is spaced by about 0.36 nm which agrees with the weak dispersive π-π stacking that holds the layers together. Ordered types of layer arrangements include the eclipsed mode, in which there is little or no layer offset, and systematic layer offset. Due to the presence of weak p-p interactions between the aromatic N-heterocyclic rings of each layer, the stacking of adjacent layers is favored over an alternated arrangement in which the energy is higher (~5 kcal/mol). However, upon stacking, a certain degree of unidirectional offset between adjacent layers was observed (~7°) owing to electrostatic repulsion between the layers. Another feature that differentiates CNDs from typical CDs is that the layers that comprise CND are not completely flat. Due to the electrostatic repulsion of the lone-pair electrons of the N atoms near the center of mass of the triple-heptazine structure, the single bond of each N atom that connects to the individual heptazines together is rotated, which bends the structure by approximately 45°.

3.5. MD simulations

Whether the structures of tau filaments vary within, or between, the brains of individuals with AD are still unknown. However, paired helical filaments (PHF) represents 80% of the tau filaments extracted from the frontal cortex of individuals with sporadic AD and are therefore the most representative structure of these aggregates [69].

The identification of the exact binding sites between CND and the tau PHF would require a high-resolution structure of the CND-PHF complex which is challenging to obtain by either NMR or X-ray diffraction (XRD) analysis. To overcome this issue, we have utilized two different molecular docking techniques (rigid and flexible docking) and MD simulations. We obtained similar results when we used a single protofilament or two packed protofilaments of the tau fibril for both techniques. In other words, there was no significant binding on the protofilament interfaces, which makes the PHF and straight filament (SF) structures of the tau fibril equal for the binding studies. The docked and MD equilibrated structure is shown in Fig. 10. In all docking poses, CND bound to the hydrophobic cavity located next to the center of mass of the individual filament. In that region, the interactions of CND and PHF were maximized due to the spherical shape of CND which allowed for interacting with a higher number of residues located in all directions around CND inside the hydrophobic cavity. In comparison, regions near the surface of PHF that possess similar amino acid sequence can only interact with one face of CND through a limited number of residues. Consequently, the CND dissociated from the surface of tau after few nanoseconds of simulation.

Inside the hydrophobic pocket, each triple-heptazine sheet is able to interact with one peptide since each sheet and each peptide were separated by about the same distance (3.5–4.5 Å) (Fig. 10). The positively charged residues LYS_{353} and LYS_{369} provide hydrogen bonding interactions with the N atoms of the heptazine rings. The neutral residues GLN_{351} and HIS_{362} interacted via hydrogen bonds with the terminal amino groups on the sheet. The hydrophobic residues ILE_{360} and ILE_{371} on the other hand, interacted with each sheet through weaker CH-π interactions. Some of the aforementioned residues were also identified as possible binding sites of tracer compounds used in positron emission tomography (PET tracer) [70]. More recently, a second generation tau PET tracer that contains 4 N-heterocyclic rings and is presently experimentally and

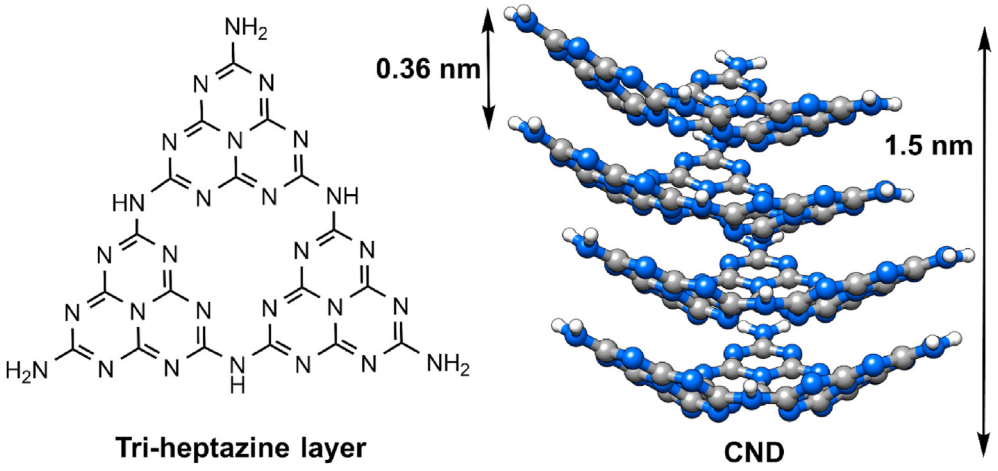

Fig. 9. Chemical structure of triple-heptazine which constitutes each layer of the CND model. The whole model with four layers and the average distance between each layer is displayed on the right.

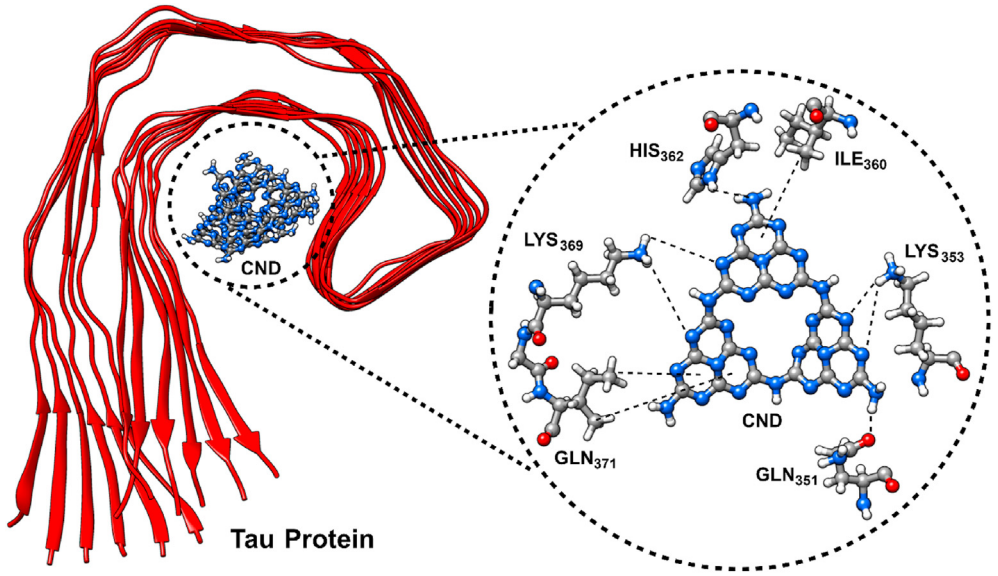

Fig. 10. MD optimized structure of tau protein-CND complex, with the nearest interacting residues shown on the right.

clinically studied was found to interact with residues in the same region as CNDs [71]. The results of these simulations are in agreement with the fact that hydrophobic CNDs are more effective in tau aggregation inhibition than the more polar isolated fractions such as F4 and F5.

3.6. ROS deactivation

In our study, ROS generation was evaluated through a photocatalytic dye degradation process. And RhB was selected since it's positively charged molecule that can efficiently interact with the negatively charged fractions. To rule out the probable photolysis, RhB was irradiated in the absence of CNDs for 1 h as control and the degradation extent of RhB was recorded in Fig. 11a, which shows that RhB couldn't self-degrade after 60 min of exposure to simulated sunlight. Subsequently, the photocatalytic system (0.6 mg of CNDs in 4 mL of RhB aqueous solution) was irradiated using a solar simulator while the absorbance at 554 nm was measured each 10 min and the obtained A/A_0 equal to C/C_0 are presented in Fig. 11a. The use of 0.6 mg of CNDs was consistent with the highest concentration of CNDs (143 μg ml^{-1}) used in MAPT experiment and the data reveal that 0.6 mg of CNDs were not able to completely degrade RhB within 60 min. Although the first 20 min witnessed degradation of RhB, the following 40 min didn't display further progress in comparison to the first 20 min. Thus, when the ROS merge with the electron deficient fractions of CNDs, the ROS electrons transfer to the surface of CNDs, and consequently the ROS are deactivated. Moreover, the photocatalytic degradation rate constant of CNDs (0.6 mg) is as low as 0.003 min^{-1} (Fig. 11b). Such low degradation rate demonstrates negligible photocatalytic reactivity and ROS induction ability of CNDs at low concentrations, which, however, is of great significance to AD patients to avoid unnecessary oxidative stress.

In addition, since CNDs were suggested to be antioxidant, to verify the hypothesis and identify the ROS suppressed by CNDs, photocatalytic experiments were conducted in RhB solutions with 12 mg of G-CDs and CD-g-C_3N_4 separately in the presence of 0.6 mg of CNDs. Based on the experimental results in our previous study,

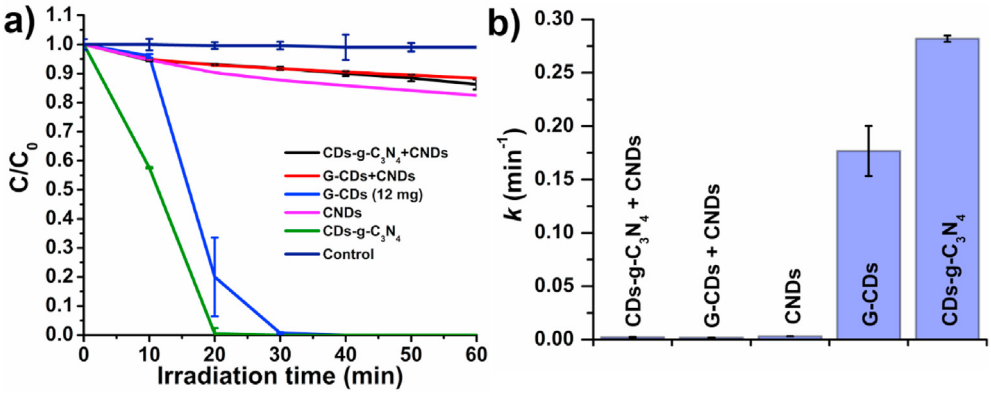

Fig. 11. Photocatalytic degradation of RhB in presence of CNDs, G-CDs or CD-g-C_3N_4. Conditions: initial RhB concentration (10 mg L^{-1}), light power (310 W), pH (neutral) and temperature (20 °C).

the major ROS induced by G-CDs and CD-g-C_3N_4 are $O_2^{\cdot-}$ and ·OH, respectively [43]. When the photocatalytic experiment was conducted using G-CDs as the sole photocatalyst in presence of CNDs (0.6 mg), the degradation rate drastically dwindled (Fig. 11b), reflecting the noteworthy effect of CNDs as a $O_2^{\cdot-}$ trap. Moreover, the photocatalytic degradation of RhB was carried out by applying CD-g-C_3N_4 as the sole photocatalyst. In the presence of CNDs (0.6 mg), a substantial reduction in the RhB degradation rate was observed in comparison to the RhB degradation rate in the absence of CNDs (Fig. 11b), indicating CNDs' suppression of ·OH. Thus, CNDs proved to be an excellent antioxidant to consume both $O_2^{\cdot-}$ and ·OH in the environment. Altogether, the ROS experiment demonstrated that CNDs (0.6 mg) wouldn't exhibit photocatalytic reactivity and induce appreciable ROS irradiated by sunlight let alone in the dark brain environment. On the contrary, CNDs would help reduce ROS especially $O_2^{\cdot-}$ and ·OH in the brain to prevent AD patients from oxidative stress.

3.7. BBB penetration

CNDs were reported to penetrate the BBB in our previous study and two mechanism hypotheses were given, namely passive diffusion or ASCT2 transporter-mediated transport [31]. To further investigate the BBB penetration mechanism of CNDs, aqueous

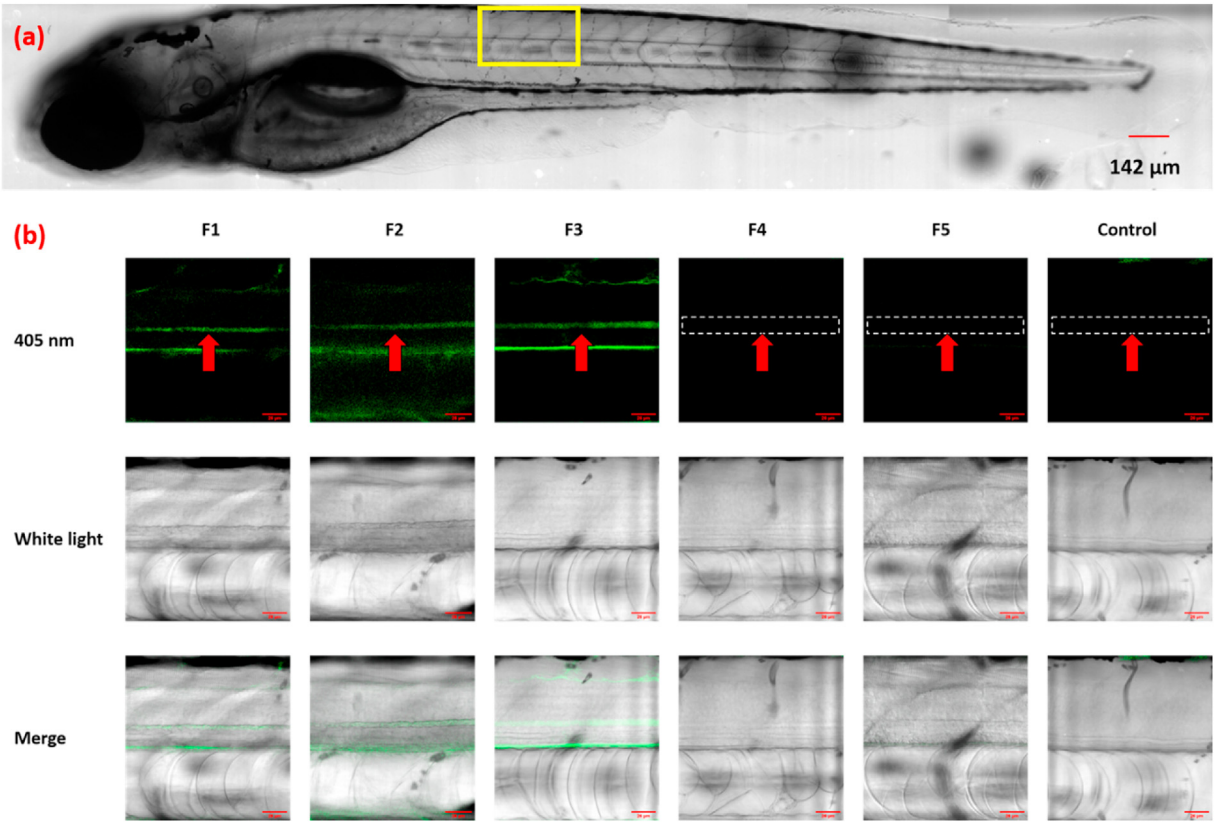

Fig. 12. Confocal images of (a) 5-dpf WT zebrafish (yellow box indicates the observation area); (b) spinal cords of zebrafish injected with aqueous solutions of CND fractions (10–50 mg/mL). The red arrows indicate the central canal of spinal cord of zebrafish.

solutions of each separated fraction with concentrations of 10–50 mg/mL were separately intravascularly injected into the heart of 5-day post-fertilization (dpf) WT zebrafish. To be specific, concentrations of F1, F3, F4 and F5 were 50 mg/mL. However, the concentration of F2 was only 10 mg/mL due to the low product yield. Under the excitation wavelength of 405 nm, the confocal images (Fig. 12) in comparison to the control demonstrate that F1, F2 and F3 could cross the BBB and reached the spinal cord which is connected to the brain by cerebral spinal fluid [30]. On the contrary, F4 and F5 failed to penetrate the BBB, which matches their higher polarity or hydrophilicity. In addition, considering similar particle sizes, electrical charges but different polarities, hydrophilicities and structures which are consistent with the BBB penetration abilities of five fractions and thanks to their good fluorescence QY, the BBB penetration mechanism of CNDs matches the passive diffusion mechanism pattern. Furthermore, previously, an ASCT2 transporter-mediated transport was also hypothesized as the BBB penetration mechanism of CNDs due to the hypothesis that the structure of CNDs resembles glutamine. However, with the content of –OH, amines, and O-containing functional groups in glutamine taken into account, which are 34% (NH_2+OH) and 50% (C=O + COOH), respectively, neither CNDs nor any separated fraction possesses similar percentages. Thus, the active route, namely ASCT2 transporter-mediated transport is ruled out while passive diffusion is preferably believed to be the sole mechanism.

4. Conclusion

Due to failure of many anti-Aβ approaches in clinical trials, MAPT becomes the next focus for AD drug discovery. It was observed that CNDs inhibit the aggregation of MAPT, a pathological hallmark of AD. In fact, CDs in general have been frequently reported for their capability to inhibit various pathological processes of neurodegeneration such as Aβ fibrillation. Furthermore, according to previous studies, it was found that inhibition of MAPT aggregation was closely associated with the chemical structure of inhibitors [72]. Thus, in order to investigate the mechanism of CNDs in the MAPT aggregation inhibition, CNDs were separated into five fractions using column chromatography. All five fractions underwent systematic characterizations and were found to share similar surface electrical properties and morphologies, but with different surface chemical structures. And the different surface contents of hydrophilic functional moieties match the increase of polarity from F1 to F5. When all the fractions together with CNDs were tested in the ThT assay for tau aggregation, higher performance in MAPT aggregation inhibition was observed with more hydrophobic fractions including F1, F2 and F3 and the highest performance was revealed with the overall CNDs, which was followed by MD simulations to confirm a hydrophobic interaction between MAPT and CNDs. Subsequently, a passive-diffusion BBB penetration mechanism of CNDs was concluded from a structure-property relationship using a zebrafish *in vivo* model. Moreover, via a photocatalytic dye degradation experiment, CNDs were observed to deactivate ROS and consume the $O_2^{\cdot-}$ and ·OH already present in the environment, which will help reduce the oxidative stress on AD patients' brains. Therefore, this study points to an innovative nanomedicine to potentially treat AD by inhibiting tau pathology and oxidative stress. Our detailed structure-function relationship exploration reveals many correlations between CND polarity, MAPT aggregation inhibition capacity, and BBB penetration ability.

There are several novel findings reported in this study. First of all, this work is the first one to report the effect of CNDs on MAPT aggregation inhibition. Secondly, with extensive literature studies, in our work, this work may be the first to create TGA chart, computational model of CNDs in combination of multiple characterization techniques and apply MD simulations to study the hydrophobic interactions between CNDs and MAPT. Thirdly, through a separation of CNDs, the structure-function relationship was discovered in the explanation of different polarities, MAPT aggregation inhibition capacities of different fractions, and the BBB penetration mechanism of the overall CNDs. Lastly, different from most CDs, the CNDs displayed an excellent ROS deactivation ability, which is of great significance in AD treatment. Therefore, taken together, this work presents a significant discovery that CNDs can be potentially used as a promising nanomedicine to treat AD from a unique viewpoint of tau pathogenesis.

CRediT authorship contribution statement

Yiqun Zhou: Conceptualization, Methodology, Validation, Formal analysis, Investigation, Data curation, Writing – original draft, Writing – review & editing, Visualization, Supervision, Project administration. **Nabin Kandel:** Validation, Investigation, Writing – original draft, Writing – review & editing, Project administration. **Mattia Bartoli:** Methodology, Validation, Formal analysis, Investigation, Writing – original draft, Writing – review & editing, Project administration. **Leonardo F. Serafim:** Methodology, Software, Validation, Formal analysis, Investigation, Writing – original draft, Writing – review & editing, Visualization, Project administration. **Ahmed E. ElMetwally:** Formal analysis, Writing – original draft, Writing – review & editing, Project administration. **Sophia M. Falkenberg:** Validation, Investigation, Writing – review & editing. **Xavier E. Paredes:** Validation, Investigation, Writing – review & editing. **Christopher J. Nelson:** Validation, Investigation. **Nathan Smith:** Validation, Investigation. **Elisa Padovano:** Validation, Investigation. **Wei Zhang:** Investigation. **Keenan J. Mintz:** Investigation, Resources, Writing – review & editing. **Braulio C.L.B. Ferreira:** Validation, Investigation. **Emel Kirbas Cilingir:** Validation, Formal analysis, Investigation. **Jiuyan Chen:** Validation, Investigation. **Sujit K. Shah:** Validation. **Rajeev Prabhakar:** Resources, Data curation, Supervision, Funding acquisition. **Alberto Tagliaferro:** Resources, Data curation, Writing – review & editing, Supervision. **Chunyu Wang:** Resources, Data curation, Writing – review & editing, Supervision, Funding acquisition. **Roger M. Leblanc:** Resources, Data curation, Writing – review & editing, Supervision, Funding acquisition.

Declaration of competing interest

The authors declare that they have no known competing financial interests or personal relationships that could have appeared to influence the work reported in this paper.

Acknowledgments

Professor Roger M. Leblanc thanks the support from National Science Foundation under the grants 1809060 and 2041413. Professor Chunyu Wang appreciates the funding (1RF1AG069039) from the National Institute on Aging. Professor Rajeev Prabhakar acknowledges the National Science Foundation under the grant (CHE-2102563). Also, authors gratefully acknowledge the great support from University of Miami, USA.

Appendix A. Supplementary data

Supplementary data to this article can be found online at https://doi.org/10.1016/j.carbon.2022.03.021.

References

[1] C. Sul-Hee, Aberrant phosphorylation in the pathogenesis of Alzheimer's disease, BMB Rep. 42 (2009) 467–474.
[2] 2015 Alzheimer's disease facts and figures, Alzheimers Dement. 11 (2015) 332–384.
[3] P.T. Francis, A.M. Palmer, M. Snape, G.K. Wilcock, The cholinergic hypothesis of Alzheimer's disease: a review of progress, J. Neurol. Neurosurg. Psychiatry 66 (1999) 137–147.
[4] A. Martorana, Z. Esposito, G. Koch, Beyond the cholinergic hypothesis: do current drugs work in Alzheimer's disease? CNS Neurosci. Ther. 16 (2010) 235–245.
[5] J. Hardy, D. Allsop, Amyloid deposition as the central event in the aetiology of Alzheimer's disease, Trends Pharmacol. Sci. 12 (1991) 383–388.
[6] N.M. Hooper, Roles of proteolysis and lipid rafts in the processing of the amyloid precursor protein and prion protein, Biochem. Soc. Trans. 33 (2005) 335–338.
[7] S. Ohnishi, K. Takano, Amyloid fibrils from the viewpoint of protein folding, Cell. Mol. Life Sci. 61 (2004) 511–524.
[8] A. Mudher, S. Lovestone, Alzheimer's disease-do tauists and baptists finally shake hands? Trends Neurosci. 25 (2002) 22–26.
[9] M. Jucker, L.C. Walker, Self-propagation of pathogenic protein aggregates in neurodegenerative diseases, Nature 501 (2013) 45–51.
[10] M.G. Bartley, K. Marquardt, D. Kirchhof, H.M. Wilkins, D. Patterson, D.A. Linseman, Overexpression of amyloid-β protein precursor induces mitochondrial oxidative stress and activates the intrinsic apoptotic cascade, J. Alzheim. Dis. 28 (2012) 855–868.
[11] S. Bhattacharya, C. Haertel, A. Maelicke, D. Montag, Galantamine slows down plaque formation and behavioral decline in the 5XFAD mouse model of Alzheimer's disease, PLoS One 9 (2014) e89454–e89465.
[12] S.D. Hettiarachchi, Y. Zhou, E. Seven, M.K. Lakshmana, A.K. Kaushik, H.S. Chand, R.M. Leblanc, Nanoparticle-mediated approaches for Alzheimer's disease pathogenesis, diagnosis, and therapeutics, J. Contr. Release 314 (2019) 125–140.
[13] F.P. Guengerich, Mechanisms of drug toxicity and relevance to pharmaceutical development, Drug Metabol. Pharmacokinet. 26 (2011) 3–14.
[14] P. Shi, M. Li, J. Ren, X. Qu, Gold nanocage-based dual responsive "caged metal chelator" release system: noninvasive remote control with near infrared for potential treatment of Alzheimer's disease, Adv. Funct. Mater. 23 (2013) 5412–5419.
[15] M.K. Gumerlock, B.D. Belshe, R. Madsen, C. Watts, Osmotic blood-brain barrier disruption and chemotherapy in the treatment of high grade malignant glioma: patient series and literature review, J. Neuro Oncol. 12 (1992) 33–46.
[16] S.-K. Wu, P.-C. Chu, W.-Y. Chai, S.-T. Kang, C.-H. Tsai, C.-H. Fan, C.-K. Yeh, H.-L. Liu, Characterization of different microbubbles in assisting focused ultrasound-induced blood-brain barrier opening, Sci. Rep. 7 (2017) 46689–46699.
[17] P.-C. Chu, W.-Y. Chai, C.-H. Tsai, S.-T. Kang, C.-K. Yeh, H.-L. Liu, Focused ultrasound-induced blood-brain barrier opening: Association with mechanical index and cavitation index analyzed by dynamic contrast-enhanced magnetic-resonance imaging, Sci. Rep. 6 (2016) 33264–33276.
[18] R.K. Upadhyay, Drug delivery systems, CNS protection, and the blood brain barrier Biomed, Res. Int. (2014), https://doi.org/10.1155/2014/869269, 2014.
[19] Y. Li, J. Bi, S. Liu, H. Wang, C. Yu, D. Li, B.-W. Zhu, M. Tan, Presence and formation of fluorescence carbon dots in a grilled hamburger, Food Funct. 8 (2017) 2558–2565.
[20] S. Mandani, D. Dey, B. Sharma, T.K. Sarma, Natural occurrence of fluorescent carbon dots in honey, Carbon 119 (2017) 569–572.
[21] Z. Wang, H. Liao, H. Wu, B. Wang, H. Zhao, M. Tan, Fluorescent carbon dots from beer for breast cancer cell imaging and drug delivery, Anal. Methods 7 (2015) 8911–8917.
[22] Y. Zhou, Z. Peng, E.S. Seven, R.M. Leblanc, Crossing the blood-brain barrier with nanoparticles, J. Contr. Release 270 (2018) 290–303.
[23] K.J. Mintz, Y. Zhou, R.M. Leblanc, Recent development of carbon quantum dots regarding their optical properties, photoluminescence mechanism, and core structure, Nanoscale 11 (2019) 4634–4652.
[24] C. Zheng, X. An, J. Gong, Novel pH sensitive N-doped carbon dots with both long fluorescence lifetime and high quantum yield, RSC Adv. 5 (2015) 32319–32322.
[25] R.E. Kellogg, R.G. Bennett, Radiationless intermolecular energy transfer. III. Determination of phosphorescence efficiencies, J. Chem. Phys. 41 (1964) 3042–3045.
[26] P.Y. Liyanage, R.M. Graham, R.R. Pandey, C.C. Chusuei, K.J. Mintz, Y. Zhou, J.K. Harper, W. Wu, A.H. Wikramanayake, S. Vanni, R.M. Leblanc, Carbon nitride dots: a selective bioimaging nanomaterial, Bioconjugate Chem. 30 (2019) 111–123.
[27] P. Zhao, B. Jin, Q. Zhang, R. Peng, High-quality carbon nitride quantum dots on photoluminescence: effect of carbon sources, Langmuir 37 (2021) 1760–1767.
[28] Y. Zhou, P.Y. Liyanage, D. Devadoss, L.R. Rios Guevara, L. Cheng, R.M. Graham, H.S. Chand, A.O. Al-Youbi, A.S. Bashammakh, M.S. El-Shahawi, R.M. Leblanc, Nontoxic amphiphilic carbon dots as promising drug nanocarriers across the blood–brain barrier and inhibitors of β-amyloid, Nanoscale 11 (2019) 22387–22397.
[29] S. Li, Z. Peng, J. Dallman, J. Baker, A.M. Othman, P.L. Blackwelder, R.M. Leblanc, Crossing the blood-brain-barrier with transferrin conjugated carbon dots: a zebrafish model study, Colloids Surf., B 145 (2016) 251–256.
[30] K.J. Mintz, G. Mercado, Y. Zhou, Y. Ji, S.D. Hettiarachchi, P.Y. Liyanage, R.R. Pandey, C.C. Chusuei, J. Dallman, R.M. Leblanc, Tryptophan carbon dots and their ability to cross the blood-brain barrier, Colloids Surf., B 176 (2019) 488–493.
[31] P.Y. Liyanage, Y. Zhou, A.O. Al-Youbi, A.S. Bashammakh, M.S. El-Shahawi, S. Vanni, R.M. Graham, R.M. Leblanc, Pediatric glioblastoma target-specific efficient delivery of gemcitabine across the blood-brain barrier via carbon nitride dots, Nanoscale 12 (2020) 7927–7938.
[32] S. Li, L. Wang, C.C. Chusuei, V.M. Suarez, P.L. Blackwelder, M. Micic, J. Orbulescu, R.M. Leblanc, Nontoxic carbon dots potently inhibit human insulin fibrillation, Chem. Mater. 27 (2015) 1764–1771.
[33] X. Han, Z. Jing, W. Wu, B. Zou, Z. Peng, P. Ren, A. Wikramanayake, Z. Lu, R.M. Leblanc, Biocompatible and blood-brain barrier permeable carbon dots for inhibition of Aβ fibrillation and toxicity, and BACE1 activity, Nanoscale 9 (2017) 12862–12866.
[34] K.J. Mintz, M. Bartoli, M. Rovere, Y. Zhou, S.D. Hettiarachchi, S. Paudyal, J. Chen, J.B. Domena, P.Y. Liyanage, R. Sampson, D. Khadka, R.R. Pandey, S. Huang, C.C. Chusuei, A. Tagliaferro, R.M. Leblanc, A deep investigation into the structure of carbon dots, Carbon 173 (2021) 433–447.
[35] P.I. Moreira, A. Nunomura, M. Nakamura, A. Takeda, J.C. Shenk, G. Aliev, M.A. Smith, G. Perry, Nucleic acid oxidation in Alzheimer disease, Free Radical Biol. Med. 44 (2008) 1493–1505.
[36] Z. An, J. Yan, Y. Zhang, R. Pei, Applications of nanomaterials for scavenging reactive oxygen species in the treatment of central nervous system diseases, J. Mater. Chem. B 8 (2020) 8748–8767.
[37] T. Zhang, J. Qu, Y. Yao, Y. Zhang, Y. Ma, D. Wu, Y. Cao, M. Yang, Y. Zhang, M. Tang, Y. Pu, N-doped carbon dots triggered the induction of ROS-mediated cytoprotective autophagy in Hepa1-6 cells, Chemosphere 251 (2020) 126440–126451.
[38] A. Nasrin, M. Hassan, V.G. Gomes, Two-photon active nucleus-targeting carbon dots: enhanced ROS generation and photodynamic therapy for oral cancer, Nanoscale 12 (2020) 20598–20603.
[39] J. Chen, S. Li, Y. Zhang, W. Wang, X. Zhang, Y. Zhao, Y. Wang, H. Bi, A reloadable self-healing hydrogel enabling diffusive transport of C-Dots across gel-gel interface for scavenging reactive oxygen species, Adv. Healthc. Mater. 6 (2017) 1700746–1700755.
[40] P. Talbiersky, F. Bastkowski, F.-G. Klärner, T. Schrader, Molecular clip and tweezer introduce new mechanisms of enzyme inhibition, J. Am. Chem. Soc. 130 (2008) 9824–9828.
[41] J. Crowe, H. Dobeli, R. Gentz, E. Hochuli, D. Stuber, K. Henco, 6xHis-Ni-NTA chromatography as a superior technique in recombinant protein expression/purification, Methods Mol. Biol. 31 (1994) 371–387.
[42] S. Sinha, D.H. Lopes, Z. Du, E.S. Pang, A. Shanmugam, A. Lomakin, P. Talbiersky, A. Tennstaedt, K. McDaniel, R. Bakshi, P.Y. Kuo, M. Ehrmann, G.B. Benedek, J.A. Loo, F.G. Klarner, T. Schrader, C. Wang, G. Bitan, Lysine-specific molecular tweezers are broad-spectrum inhibitors of assembly and toxicity of amyloid proteins, J. Am. Chem. Soc. 133 (2011) 16958–16969.
[43] Y. Zhou, A.E. ElMetwally, J. Chen, W. Shi, E.K. Cilingir, B. Walters, K.J. Mintz, C. Martin, B.C.L.B. Ferreira, W. Zhang, S.D. Hettiarachchi, L.F. Serafim, P.L. Blackwelder, A.H. Wikramanayake, Z. Peng, R.M. Leblanc, Gel-like carbon dots: a high-performance future photocatalyst, J. Colloid Interface Sci. 599 (2021) 519–532.
[44] Y. Zhou, K.J. Mintz, C.Y. Oztan, S.D. Hettiarachchi, Z. Peng, E.S. Seven, P.Y. Liyanage, S. De La Torre, E. Celik, R.M. Leblanc, Embedding carbon dots in superabsorbent polymers for additive manufacturing, Polymers 10 (2018) 921–932.
[45] Y. Zhou, E.M. Zahran, B.A. Quiroga, J. Perez, K.J. Mintz, Z. Peng, P.Y. Liyanage, R.R. Pandey, C.C. Chusuei, R.M. Leblanc, Size-dependent photocatalytic activity of carbon dots with surface-state determined photoluminescence, Appl. Catal., B 248 (2019) 157–166.
[46] Y. Zhang, P. Zhuo, H. Yin, Y. Fan, J. Zhang, X. Liu, Z. Chen, Solid-state fluorescent carbon dots with aggregation-induced yellow emission for white light-emitting diodes with high luminous efficiencies, ACS Appl. Mater. Interfaces 11 (2019) 24395–24403.
[47] Y. Zhou, P.Y. Liyanage, D.L. Geleroff, Z. Peng, K.J. Mintz, S.D. Hettiarachchi, R.R. Pandey, C.C. Chusuei, P.L. Blackwelder, R.M. Leblanc, Photoluminescent carbon dots: a mixture of heterogeneous fractions, ChemPhysChem 19 (2018) 2589–2597.
[48] N.T. Silva, N.F. Nascimento, L.S. Cividanes, C.A. Bertran, G.P. Thim, Kinetics of cordierite crystallization from diphasic gels, J. Sol. Gel Sci. Technol. 47 (2008) 140–147.
[49] L. Stradella, M. Argentero, A study of the thermal decomposition of urea, of related compounds and thiourea using DSC and TG-EGA, Thermochim. Acta 219 (1993) 315–323.
[50] G. Huang, X. Chen, C. Wang, H. Zheng, Z. Huang, D. Chen, H. Xie, Photoluminescent carbon dots derived from sugarcane molasses: synthesis, properties, and applications, RSC Adv. 7 (2017) 47840–47847.
[51] A. Mewada, S. Pandey, M. Thakur, D. Jadhav, M. Sharon, Swarming carbon dots for folic acid mediated delivery of doxorubicin and biological imaging, J. Mater. Chem. B 2 (2014) 698–705.
[52] S. Tischer, M. Börnhorst, J. Amsler, G. Schoch, O. Deutschmann, Thermodynamics and reaction mechanism of urea decomposition, Phys. Chem. Chem. Phys. 21 (2019) 16785–16797.

[53] D. Wang, Z. Wang, Q. Zhan, Y. Pu, J.-X. Wang, N.R. Foster, L. Dai, Facile and scalable preparation of fluorescent carbon dots for multifunctional applications, Engineering 3 (2017) 402–408.
[54] A. Mewada, S. Pandey, S. Shinde, N. Mishra, G. Oza, M. Thakur, M. Sharon, M. Sharon, Green synthesis of biocompatible carbon dots using aqueous extract of Trapa bispinosa peel, Mater. Sci. Eng. C 33 (2013) 2914–2917.
[55] G. Zhang, M. Wen, S. Wang, J. Chen, J. Wang, Insights into thermal reduction of the oxidized graphite from the electro-oxidation processing of nuclear graphite matrix, RSC Adv. 8 (2018) 567–579.
[56] J. Li, D. Liu, B. Li, J. Wang, S. Han, L. Liu, H. Wei, A bio-inspired nacre-like layered hybrid structure of calcium carbonate under the control of carboxyl graphene, CrystEngComm 17 (2015) 520–525.
[57] C. Li, Q. Ran, R. Zhu, Y. Gu, Study on thermal degradation mechanism of a cured aldehyde-functional benzoxazine, RSC Adv. 5 (2015) 22593–22600.
[58] N. Ravi, S.A. Anuar, N.Y.M. Yusuf, W.N.R.W. Isahak, M.S. Masdar, Amine-mixed oxide hybrid materials for carbon dioxide adsorption from CO_2/H_2 mixture, Mater. Res. Express 5 (2018) 55501–55514.
[59] H. Dai, X. Gao, E. Liu, Y. Yang, W. Hou, L. Kang, J. Fan, X. Hu, Synthesis and characterization of graphitic carbon nitride sub-microspheres using microwave method under mild condition, Diam. Relat. Mater. 38 (2013) 109–117.
[60] L.-Y. Chen, W.-D. Zhang, $In_2O_3/g\text{-}C_3N_4$ composite photocatalysts with enhanced visible light driven activity, Appl. Surf. Sci. 301 (2014) 428–435.
[61] Z.-l. Wang, D. Xu, Y. Huang, Z. Wu, L.-m. Wang, X.-b. Zhang, Facile, mild and fast thermal-decomposition reduction of graphene oxide in air and its application in high-performance lithium batteries, Chem. Commun. 48 (2012) 976–978.
[62] Y. Bleu, V. Barnier, F. Christien, F. Bourquard, A.S. Loir, F. Garrelie, C. Donnet, Dynamics of carbon diffusion and segregation through nickel catalyst, investigated by in-situ XPS, during the growth of nitrogen-doped graphene, Carbon 155 (2019) 410–420.
[63] A. Lerf, H. He, T. Riedl, M. Forster, J. Klinowski, ^{13}C and ^{1}H MAS NMR studies of graphite oxide and its chemically modified derivatives, Solid State Ionics 101–103 (1997) 857–862.
[64] F.P.G.d. Arquer, D.V. Talapin, V.I. Klimov, Y. Arakawa, M. Bayer, E.H. Sargent, Semiconductor quantum dots: Technological progress and future challenges, Science 373 (2021) eaaz8541–eaaz8556.
[65] A. Fardanesh, S. Zibaie, B. Shariati, F. Attar, F. Rouhollah, K. Akhtari, K. Shahpasand, A.A. Saboury, M. Falahati, Amorphous aggregation of tau in the presence of titanium dioxide nanoparticles: biophysical, computational, and cellular studies, Int. J. Nanomed. 14 (2019) 901–911.
[66] T.S. Miller, A.B. Jorge, T.M. Suter, A. Sella, F. Corà, P.F. McMillan, Carbon nitrides: synthesis and characterization of a new class of functional materials, Phys. Chem. Chem. Phys. 19 (2017) 15613–15638.
[67] G. Chen, Z. Zhang, W. Zhang, L. Xia, X. Nie, W. Huang, X. Wang, L. Wang, C. Hong, Z. Zhang, Y. You, Photopolymerization performed under dark conditions using long-stored electrons in carbon nitride, Mater. Horiz. 8 (2021) 2018–2024.
[68] M. Paloncýová, M. Langer, M. Otyepka, Structural dynamics of carbon dots in water and N,N-dimethylformamide probed by all-atom molecular dynamics simulations, J. Chem. Theor. Comput. 14 (2018) 2076–2083.
[69] B. Falcon, W. Zhang, M. Schweighauser, A.G. Murzin, R. Vidal, H.J. Garringer, B. Ghetti, S.H.W. Scheres, M. Goedert, Tau filaments from multiple cases of sporadic and inherited Alzheimer's disease adopt a common fold, Acta Neuropathol. 136 (2018) 699–708.
[70] N.A. Murugan, A. Nordberg, H. Ågren, Different positron emission tomography tau tracers bind to multiple binding sites on the tau fibril: insight from computational modeling, ACS Chem. Neurosci. 9 (2018) 1757–1767.
[71] G. Kuang, N.A. Murugan, Y. Zhou, A. Nordberg, H. Ågren, Computational insight into the binding profile of the second-generation PET tracer PI2620 with tau fibrils, ACS Chem. Neurosci. 11 (2020) 900–908.
[72] M. Okuda, I. Hijikuro, Y. Fujita, T. Teruya, H. Kawakami, T. Takahashi, H. Sugimoto, Design and synthesis of curcumin derivatives as tau and amyloid β dual aggregation inhibitors, Bioorg. Med. Chem. Lett 26 (2016) 5024–5028.